Bioorganic Chemistry 88 (2019) 102893

Contents lists available at ScienceDirect

Bioorganic Chemistry

journal homepage: www.elsevier.com/locate/bioorg

Probing the high potency of pyrazolyl pyrimidinetriones and thioxopyrimidinediones as selective and efficient non-nucleotide inhibitors of recombinant human ectonucleotidases

Hina Andleeb[a,b], Shahid Hameed[a,*], Syeda Abida Ejaz[c], Imtiaz Khan[a,d,e], Sumera Zaib[c], Joanna Lecka[f,g], Jean Sévigny[f,g], Jamshed Iqbal[c,*]

[a] Departmentof Chemistry, Quaid-i-Azam University, 45320 Islamabad, Pakistan
[b] Sulaiman Bin Abdullah Aba Al-Khail – Centre for Interdisciplinary Research in Basic Science (SA-CIRBS), Faculty of Basic and Applied Sciences, International Islamic University, Islamabad, Pakistan
[c] Centre for Advanced Drug Research, COMSATS Institute of Information Technology, Abbottabad 22060, Pakistan
[d] School of Chemistry, The University of Manchester, Oxford Road, Manchester M13 9PL, United Kingdom
[e] Manchester Institute of Biotechnology, The University of Manchester, 131 Princess Street, Manchester M1 7DN, United Kingdom
[f] Département de microbiologie-infectiologie et d'immunologie, Faculté de Médecine, Université Laval, Québec, QC G1V 0A6, Canada
[g] Centre de Recherche du CHU de Québec – Université Laval, Québec, QC G1V 4G2, Canada

ARTICLE INFO

Keywords:
Pyrazole
Pyrimidinetriones
Thioxopyrimidinediones
Recombinant enzymes
Ectonucleotidases
Alkaline phosphatatses, biological screening

ABSTRACT

With the aim to discover novel, efficient and selective inhibitors of human alkaline phosphatase and nucleotide pyrophosphatase enzymes, two new series of pyrazolyl pyrimidinetriones (PPTs) (**6a–g**) and thioxopyrimidinediones (PTPs) (**6h–n**) were synthesized in good chemical yields using Knoevenagel condensation reaction between pyrazole carbaldehydes (**4a–g**) and pharmacologically active *N*-alkylated pyrimidinetrione (**5a**) and thioxopyrimidinedione (**5b**). The inhibition potential of the synthesized hybrid compounds was evaluated against human alkaline phosphatase (*h*-TNAP and *h*-IAP) and ectonucleotidase (*h*-NPP1 and *h*-NPP3) enzymes. Most of the tested analogs were highly potent with a variable degree of inhibition depending on the functionalized hybrid structure. The detailed structure-activity relationship (SAR) of PPT and PTP derivatives suggested that the compound with unsubstituted phenyl ring from PPT series led to selective and potent inhibition (**6a**; IC_{50} = 0.33 ± 0.02 μM) of *h*-TNAP, whereas compound **6c** selectively inhibited *h*-IAP isozyme with IC_{50} value of 0.86 ± 0.04 μM. Similarly, compounds **6b** and **6h** were identified as the lead scaffolds against *h*-NPP1 and h-NPP3, respectively. The probable binding modes for the most potent inhibitors were elucidated through molecular docking analysis. Structure-activity relationships, mechanism of action, cytotoxic effects and druglikeness properties are also discussed.

1. Introduction

Ecto-nucleotidases (neucleotide metabolizing enzymes) modulate P2 purinergic signaling [1] and are responsible for maintaining cell function. Overexpression of a number of these ubiquitous ecto-enzymes has been involved in a variety of disorders [1] including cell activation, adhesion, apoptosis, proliferation and degenerative neurological and immunological responses. Selective inhibition of ecto-enzymes is an area that is currently being explored with immense interest and may prove to result in many beneficial therapeutic implications.

Ecto-nucleotide pyrophosphatases/phosphodiesterases (NPPs) belong to metalloenzyme family and comprise seven different subtypes (NPP1-7). Among different isozymes, the literature data explicitly reveals the prominence and applications of only three members, *i.e.* NPP1-3 [1,2]. Both NPP1 and NPP3 perform the hydrolysis of pyrophosphates and phosphodiesters in various nucleotides and their derivatives [2]. In addition, these isozymes are also capable of hydrolyzing the artificial phosphoric acid esters [2–4]. They either exist as trans-membrane glycoproteins or secreted proteins [3,4]. NPP1-3 are substrate specific and are widely expressed in various tissues. They have been associated with multiple physiological functions including extracellular pyrophosphate levels regulation, nucleotide recycling, stimulating cell motility and modulation of purinergic receptor signaling [5]. The main substrate of NPPs is adenosine triphosphate (ATP),

* Corresponding authors.
E-mail addresses: shameed@qau.edu.pk (S. Hameed), drjamshed@ciit.net.pk (J. Iqbal).

https://doi.org/10.1016/j.bioorg.2019.03.067
Received 5 September 2018; Received in revised form 19 March 2019; Accepted 25 March 2019
Available online 02 April 2019
0045-2068/

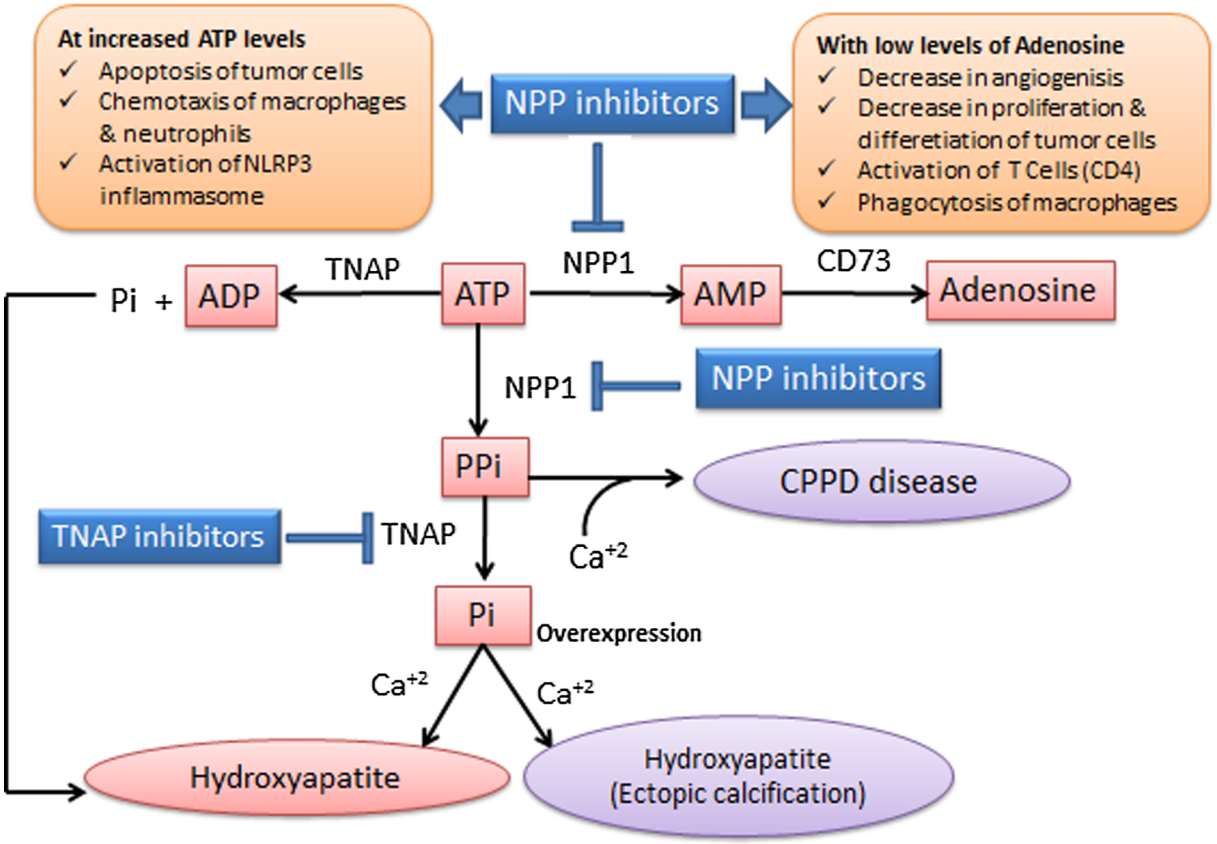

Fig. 1. Work pathway for NPP1 and TNAP, the pathologies associated with their overexpression and the effect of inhibitors on their work pathway.

which is cleaved to adenosine monophosphate (AMP) and diphosphate (ADP) or pyrophosphate (ppi) (Fig. 1). Specifically, NPP1 is involved in various biological processes including insulin receptor signaling, bone mineralization and immune modulation. Its overexpression leads to ectopic calcification (pathologic deposition of calcium salts in tissues), calcium pyrophosphate dihydrate crystal deposition (CPPD) and cancer cell proliferation, whereas NPP3 is suggested as a tumor marker since its expression has been associated with carcinogenesis and cancer cell metastasis [6]. NPP1 inhibitors have potential as novel drugs, *e.g.* for (immuno)oncology. The blockade of NPP1 can increase the concentration of ATP, however, at the same time it can decrease the concentration of adenosine by reducing the concentration of its precursor, adenosine monophosphate (Fig. 1). This may lead to an enhancement of the immune response in the body [7]. To date, the reported NPP inhibitors have been recognized as non-selective inhibitors of various ecto-nucleotidases [8]. Therefore, selective and potent NPP inhibitors for the treatment of several disorders, *i.e.* cancer or chondrocalcinosis caused by calcium pyrophosphate dihydrate crystal deposition disease (CPPD), are desired to be explored.

Alkaline phosphatases (APs, EC 3.1.3.1) on the other hand, are well-studied homodimeric metallo-enzymes that catalyze dephosphorylation of nucleoside phosphates and phosphomonoesters [9,10]. In APs, catalytic active site is situated on the external cell surface *via* a glycosyl-phosphatidyl inositol (GPI) anchor making them ideal drug targets, since potential drug molecules do not necessarily have to be cell-permeable in order to induce the desired physiological effects [11]. This isozyme family is broadly categorized into two groups, namely: tissue-nonspecific alkaline phosphatases (TNAP) and tissue-specific alkaline phosphatases (placental, intestinal and germ cell). Although the mammalian alkaline phosphatases display low sequence similarity with the *E. coli* enzyme (25–30%), the active site containing divalent metals ions remains highly conserved producing a catalytic activity similar to alkaline phosphatases of *E. coli* and eukaryotes [12,13]. The overexpression of human alkaline phosphatases in various tumor cells has been shown recently [14]. Increased levels of plasma TNAP were observed in Paget's disease [15], osteosarcomas [16] and osteoblastic bone metastasis [17].

Increased circulating expression of alkaline phosphatase has a crucial role in vascular calcification due to imbalance between inhibitors and promoters of mineralization [18]. Overexpression of TNAP is associated with high rates of mortality and cardiovascular events *via* mechanisms that involve endothelial dysfunction, vascular calcification and inflammation (Fig. 2). Interventional strategies to lower TNAP activity include direct alkaline phosphatase inhibitors, vitamin D analogues and calcimimetic molecules [18]. Intestinal alkaline phosphatases (IAPs) regulate the intestinal lipid absorption, bicarbonate secretion and maintain the pH of duodenal surface along with detoxification of bacterial lipopolysaccharide (LPS) [19]. High levels of intestinal-type alkaline phosphatase (IAP) and TNAP, owing to sepsis and acute inflammation, can lead to endotoxin and nucleotide detoxification and cytokine inactivation [18].

Although, the inhibition of TNAP is largely achieved by a limited number of small molecules including levamisole, theophylline and L-homoarginine, the selectivity issue still persists [20]. Development of selective alkaline phosphatase inhibitors is a potential strategy to reduce vascular calcification and improve cardiovascular outcomes in patients with chronic kidney disease (CKD) or type 2 diabetes mellitus. The aforementioned therapeutic potential of both ecto-nucleotide pyrophosphatases and alkaline phosphatase isozymes as prospective drug targets, and the lack of meaningful structure-activity relationship and enzyme selectivity data for both families, encouraged us to design fundamental motifs and synthesize new series of unexplored molecules with potent and selective inhibitory effects.

Among five-membered bioactive heterocycles, pyrazoles have

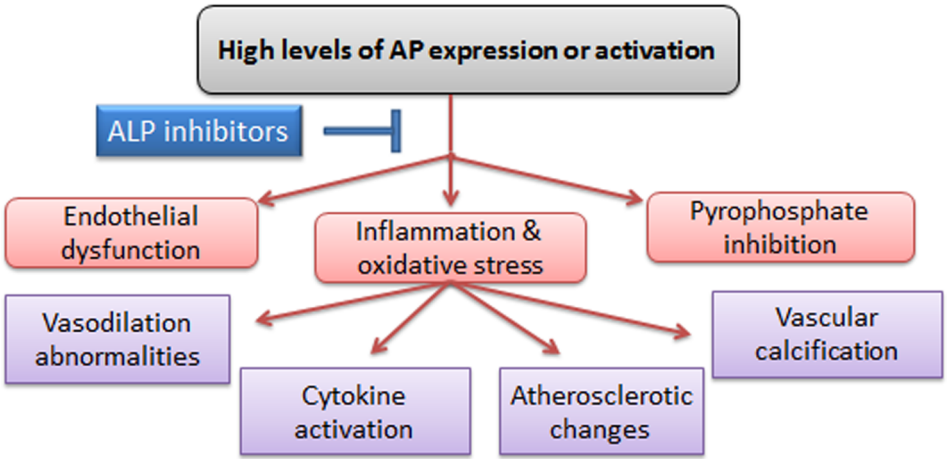

Fig. 2. Pathological effects of overexpression of APs.

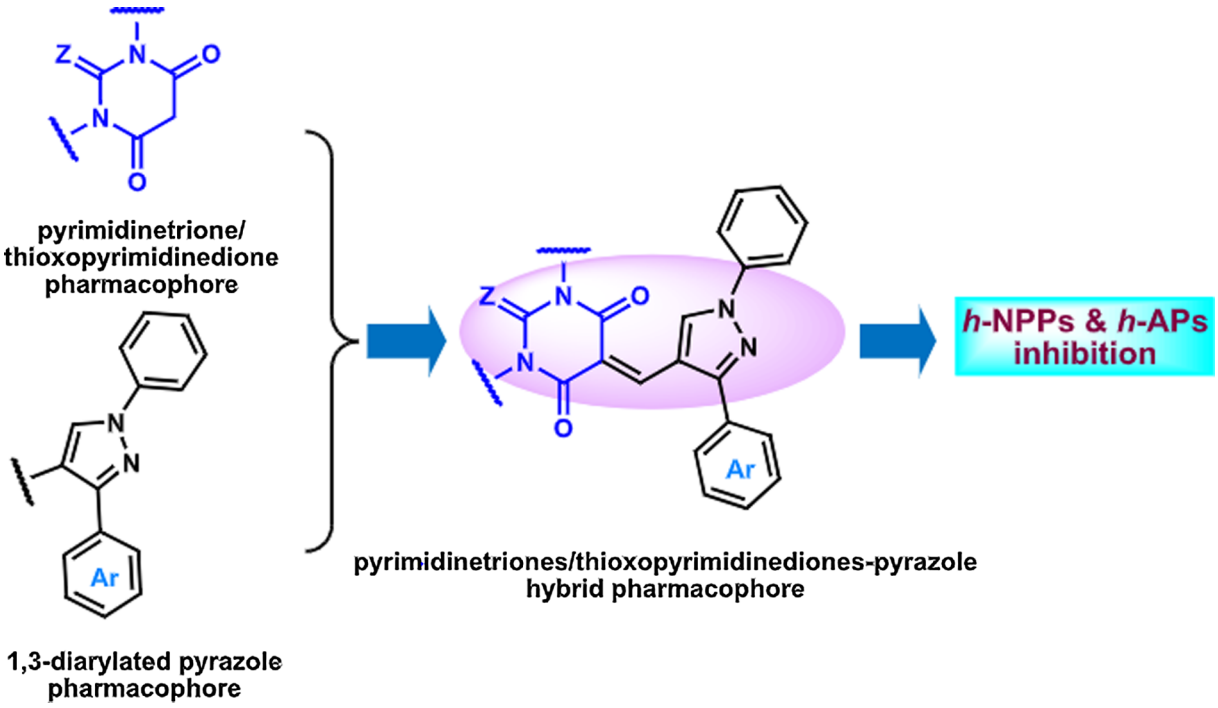

Fig. 3. A pharmacophore integrated approach for the structural design of pyrazolyl pyrimidinetrione and thioxopyrimidinedione conjugates.

maintained a unique and dominant position due to their presence as key structural unit in several pharmaceutical drugs, such as rimonabant and celecoxib [21]. Pyrazoles are also present in many natural products including pyrazofurin, formycin, oxoformycin B and nostocine [22]. They show a diverse range of biological properties such as anti-hyperglycemic [23], anti-inflammatory [24], anti-cancer [25a–25c], anti-viral [26a,26b] and anti-microbial activities [27]. Recently, pyrazoles have been reported as promising candidates for the inhibition of ecto-nucleotidases [28]. Pyrimidinetriones and 2-thioxopyrimidinediones, on the other hand, are versatile poly-functional molecules containing five potential metal binding sites (lone pairs on three oxygen and two nitrogen atoms in case of pyrimidinetriones; while on two oxygen, one sulfur and two nitrogen atoms in case of 2-thioxopyrimidinediones) and are supposed to be suitable to anchor these metallo-enzymes. Therefore, we designed novel heterocyclic entities incorporating pyrimidinetriones/thioxopyrimidinediones and pyrazoles, endowed with several exploitable and diversified functional groups. Using the pharmacophore integration approach, we successfully coupled the two bioactive nuclei delivering a unique set of hybrid compounds (Fig. 3), which to the best of our knowledge, has not been reported previously. We herein report a high yielding synthesis for 1-phenyl-3-arylpyrazol-4-yl-5-methylene-*N,N′*-dialkylpyrimidine-2,4,6-triones (PPTs) and 1-phenyl-3-arylpyrazol-4-yl-5-methylene-*N,N′*-dialkyl-2-thioxopyrimidine-4,6-diones (PTPs) with three potential sites for structural modifications. The notable features of our approach include the generation of varied structures in good to excellent purified yields from easily accessible starting materials. *In vitro* assays for nucleotide pyrophosphatase and alkaline phosphatase inhibition were performed to analyze the biological potential of the newly synthesized compounds, and the acquired results were rationalized with the help of molecular docking investigations.

2. Results and discussion

2.1. Chemistry

The practical route to the synthesis of pyrazolyl pyrimidinetrione and thioxopyrimidinedione hybrid compounds (**6a–n**) is illustrated in Scheme 1. The synthesis of key pyrazole fragment (**4a–g**) was achieved

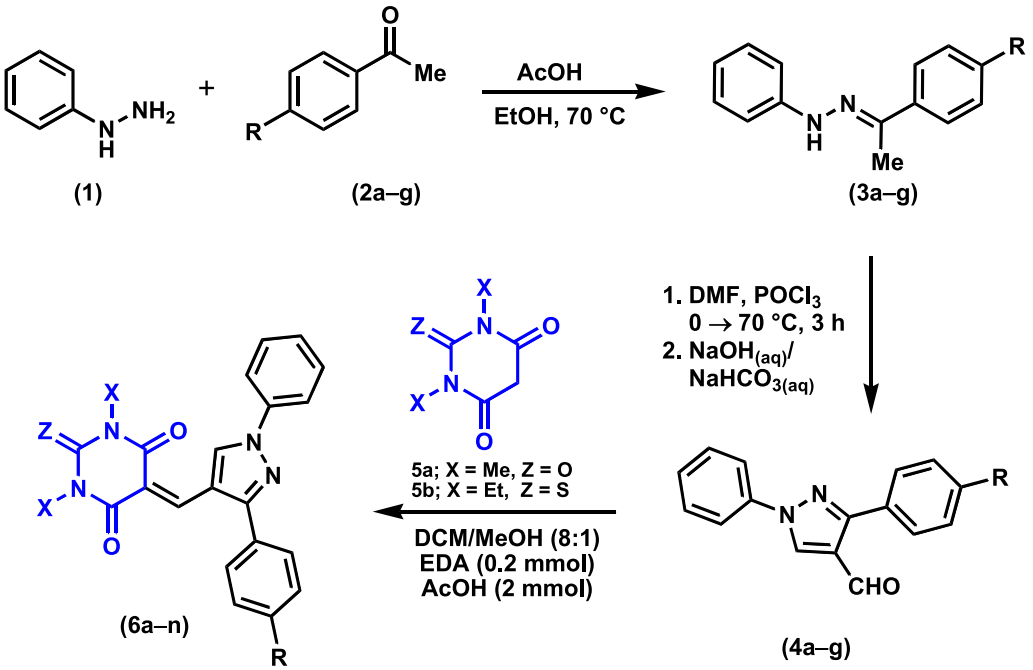

6a:	X = Me, Z = O, R = H	**6h:**	X = Et, Z = S, R = H
6b:	X = Me, Z = O, R = F	**6i:**	X = Et, Z = S, R = F
6c:	X = Me, Z = O, R = Cl	**6j:**	X = Et, Z = S, R = Cl
6d:	X = Me, Z = O, R = Br	**6k:**	X = Et, Z = S, R = Br
6e:	X = Me, Z = O, R = Me	**6l:**	X = Et, Z = S, R = Me
6f:	X = Me, Z = O, R = OMe	**6m:**	X = Et, Z = S, R = OMe
6g:	X = Me, Z = O, R = NO_2	**6n:**	X = Et, Z = S, R = NO_2

Scheme 1. Synthetic pathway to pyrazolyl pyrimidinetriones (PPTs) and thioxopyrimidinediones (PTPs).

in two steps. Initially, the reaction of phenylhydrazine (**1**) with 4-substituted acetophenones (**2a–g**) afforded phenylhydrazones (**3a–g**) under acidic conditions. Subsequently, the Vilsmeier–Haack formylation reaction of phenylhydrazones (**3a–g**) provided a facile access to corresponding 4-carboxaldehyde functionalized pyrazole derivatives (**4a–g**). The reaction was performed using 3 equivalents of Vilsmeier–Haack reagent (DMF-$POCl_3$), followed by treatment with cold aqueous base (NaOH or $NaHCO_3$) delivering a diversified series of 3-aryl-1*H*-pyrazole-4-carbaldehydes (**4a–g**) in good to excellent yields [29].

1-Phenyl-3-aryl-1*H*-pyrazole-4-carbaldehydes (**4a–g**) were coupled to *N*-alkylated pyrimidinetriones (**5a**) and thioxopyrimidinediones (**5b**) under previously developed conditions [29] of Knoevenagel condensation reaction to deliver the range of 1-phenyl-3-arylpyrazol-4-yl-5-methylene-*N,N′*-dialkylpyrimidine-2,4,6-triones (PPTs) (**6a–g**) and 1-phenyl-3-arylpyrazol-4-yl-5-methylene-*N,N′*-dialkyl-2-thioxopyrimidine-4,6-diones (PTPs) (**6h–n**). This simple methodology proved to be quite general: unsubstituted and 4-substituted aryl moieties with both electron-rich (methyl, methoxy) and electron-poor (fluoro, chloro, bromo, nitro) substituents attached to position 3 of the pyrazole fragment afforded the desired hybrid compounds in good to excellent yields. In addition, small alkyl groups (methyl and ethyl) attached to nitrogen atom of pyrimidinetrione and thioxopyrimidinedione components were also well tolerated.

All the synthesized compounds were characterized by readily available analytical methods including FTIR, ^{1}H and ^{13}C NMR spectroscopy and mass spectrometry. In IR spectra of compounds **6a–n**, the stretching vibrations observed in the range 1623–1563 cm^{-1} were attributed to C═N functionality (pyrazole), while the strong bands for carbonyl stretching frequencies appeared in the region 1710–1698 cm^{-1}. In ^{1}H NMR spectra, the most characteristic olefinic proton (═C–H) resonated in the range of 8.85–8.28 ppm, whereas the ═C–H proton of the pyrazole ring appeared in the region 9.96–9.70 ppm. ^{13}C NMR spectra showed diagnostic chemical shifts in the region of 179.81–178.45 ppm due to the presence of C═S in case of thioxopyrimidinediones **(6h–n)**, whereas the C═O functional groups in the synthesized compounds resonated from 165.90 to 158.61 ppm. Finally, elemental analysis was used to ascertain the purity of the target compounds (**6a–n**).

2.2. Enzyme inhibition studies and structure-activity relationship analysis

To analyze the biological properties of newly synthesized library of 1-phenyl-3-arylpyrazol-4-yl-5-methylene-*N,N′*-dialkylpyrimidine-2,4,6-triones (PPTs) (**6a–g**) and 1-phenyl-3-arylpyrazol-4-yl-5-methylene-*N,N′*-dialkyl-2-thioxopyrimidine-4,6-diones (PTPs) (**6h–n**), *in vitro* inhibitory potency was measured against *h*-APs and *h*-NPPs. The biological inhibition results are summarized in Table 1.

Most of the derivatives of both the synthesized series exhibited dual inhibition of isozymes of APs and NPPs, but with more selectivity towards *h*-APs. Interestingly, in the alkaline phosphatase assay, compounds **6a**, **6b**, **6e**, **6h** and **6k** with pronounced inhibition against *h*-TNAP were inactive against *h*-IAP (except **6l** and **6n**) and *vice versa*. These inhibition results explicitly address the selectivity issues. The detailed structure-activity relationship of PPT and PTP derivatives against APs suggested that the unsubstituted phenyl ring in case of PPT led to a potent inhibitor (**6a**; IC_{50} = 0.33 ± 0.02 μM) of *h*-TNAP. Compound **6a** exhibited ~60-fold stronger inhibition than the reference drug (levamisole: IC_{50} = 20.2 ± 1.21 μM). On the other hand, the unsubstituted derivative of PTPs (**6h**) exhibited less inhibitory potential towards *h*-TNAP compared to compound **6a**. Compound **6c** was identified as the most potent and selective inhibitor of *h*-IAP with IC_{50} value of 0.86 ± 0.04 μM unveiling ~116-fold higher inhibition than the reference compound (L-phenylalanine; IC_{50} = 100 ± 3.01 μM).

Table 1
Alkaline phosphatase (*h*-TNAP & *h*-IAP) and nucleotide pyrophosphatase (*h*-NPP1 & h-NPP3) inhibition data for compounds **6a–n**.

Compound	*h*-TNAP	*h*-IAP	*h*-NPP1	*h*-NPP3
	IC_{50} (μM) ± SEM			
6a	0.33 ± 0.02	> 100	> 100	1.36 ± 0.31
6b	2.21 ± 0.24	> 100	0.61 ± 0.05	0.66 ± 0.04
6c	> 100	0.86 ± 0.04	> 100	> 100
6d	> 100	1.57 ± 0.32	1.21 ± 0.22	2.27 ± 0.11
6e	5.83 ± 0.78	> 100	1.86 ± 0.31	> 100
6f	> 100	> 100	> 100	> 100
6g	> 100	12.7 ± 1.45	> 100	2.49 ± 0.28
6h	2.99 ± 0.18	> 100	4.61 ± 0.32	0.57 ± 0.01
6i	> 100	> 100	> 100	2.03 ± 0.02
6j	> 100	33.6 ± 3.45	1.01 ± 0.03	> 100
6k	3.07 ± 0.24	> 100	> 100	6.36 ± 0.18
6l	5.26 ± 1.09	6.33 ± 0.34	> 100	4.55 ± 0.17
6m	> 100	1.31 ± 0.32	> 100	2.86 ± 0.18
6n	1.78 ± 0.34	21.2 ± 2.56	> 100	2.11 ± 0.13
Suramin	—	—	8.67 ± 1.31	1.27 ± 0.82
Levamisole	20.2 ± 1.21	—	—	—
L-Phenylalanine	—	100 ± 3.02	—	—

The higher inhibitory potential of this compound could be attributed to the presence of an inductively withdrawing chloro substituent at the para-position of the phenyl ring attached to the pyrazole core. However, comparatively lower activity (IC_{50} = 1.57 ± 0.32 μM) was observed for **6d** incorporating a bromine atom at the same position. A striking difference was observed when compound **6c** was compared to its thioxo analog **(6j)** where lower activity (33.6 ± 3.45 μM) was observed for compound **6j**. However, activity was almost restored (1.31 ± 0.32 μM) when chloro group was replaced by a methoxy substituent in compound **6m**. A similar trend was observed in case of PTP derivatives (**6h–n**) where compound **6j** showed higher inhibition (IC_{50} = 33.6 ± 3.45 μM) compared to its fluoro **(6i)** and bromo analogs **(6k)**. It was also observed that compound **6b** bearing fluorine substituent at the phenyl ring showed stronger and selective inhibitory potential towards *h*-TNAP. In case of compound **6e** bearing electron-donating methyl group, selective inhibition was also observed towards *h*-TNAP, whereas compound **6g** featuring a polarized nitro group, showed selective and efficient inhibition of *h*-IAP with an IC_{50} value of 12.7 ± 1.45 μM. Based on these inhibitory results, it could be reasonably suggested that the presence of appropriate substituent at aromatic moiety of pyrazole and the coupled pyrimidinetrione/thioxopyrimidinedione is the key combination for high profile selective

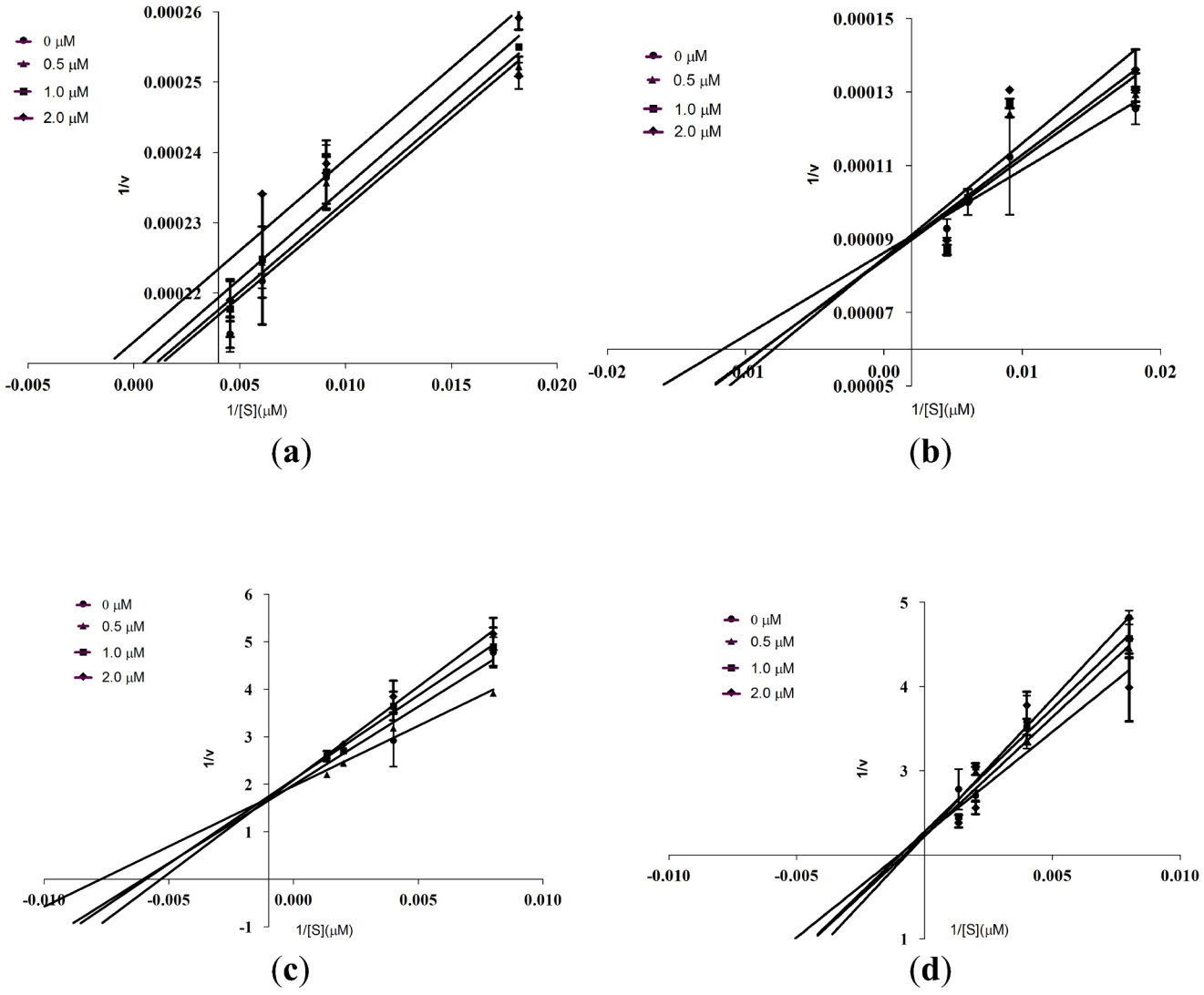

Fig. 4. . Lineweaver-Burk plot for *h*-TNAP and *h*-IAP inhibition by compounds **6a** (a); and **6c** (b) where S is concentration of substrate CDP-star® (μM). Lineweaver-Burk plot for *h*-NPP1 and *h*-NPP3 inhibition by compound **6b** (c); and **6h** (d) where S is concentration of substrate *p*-Nph-TMP (μM).

inhibition of *h*-IAP and *h*-TNAP isozymes.

On the other hand, when the structure-activity relationship of PPT and PTP derivatives was studied towards *h*-NPPs, it was observed that these derivatives exhibited more inhibitory potential towards *h*-NPP1 as compared to *h*-NPP3. The bioactivity results of these derivatives suggested that the derivatives **6b** from PPT and **6j** from PTP series bearing F and Cl atom at 4 position of phenyl ring, respectively, exhibited maximum inhibitory potential towards *h*-NPP3. It was also notable to perceive that compound **6h** displayed 2-fold higher inhibition (IC_{50} = 0.57 ± 0.01 μM) of *h*-NPP3 compared to suramin (positive control) (IC_{50} = 1.27 ± 0.08 μM). Compound **6b** also revealed ~14-fold higher inhibitory values towards *h*-NPP1 as compared to standard inhibitor, whereas 2-fold stronger inhibition of *h*-NPP3 was observed. Compounds **6e** also unveiled selective and efficient inhibition of *h*-NPP1 with IC_{50} values of 1.86 ± 0.31 μM. Moreover, compounds **6a**, **6g** and **6i** and compounds **6k–n** exhibited relatively lower inhibition of *h*-NPP3 but with complete selectivity.

In general, the analyzed compounds revealed a remarkable inhibition profile against recombinant human ectonucleotidases identifying several leads with excellent levels of selectivity.

2.3. Molecular docking studies

The binding mode of the selective and potent inhibitors against *h*-TNAP, *h*-IAP, *h*-NPP1 and *h*-NPP3 were docked inside the active site of the respective enzymes. Due to the unavailability of crystal structures in the protein data bank, the homology models were generated by our research group [30–32] and molecular docking was performed. As the newly generated models do not contain any cognate ligand inside the active pocket, therefore, the MOE site finder was used to search and select the binding of protein. For the validation purpose, the reference compounds used as standards in biological assays were docked within the binding site of protein before carrying out further docking. The putative interactions were analyzed and compared. The presence of Zinc ions within active center was important for the interaction and binding of the inhibitors. The putative binding interactions of standard compounds are depicted in Figs. 4a, 5a, 6c and 7c against *h*-TNAP, *h*-IAP, *h*-NPP1 and *h*-NPP3, respectively.

The results of biological studies suggested that compound **6a** was the potent and selective inhibitor for *h*-TNAP, whereas compound **6c** emerged as selected and potent inhibitor for *h*-IAP. Moreover, for *h*-NPP3, the most potent compound was found to be **6h**. Compound **6b** not only showed potent inhibition against *h*-NPP1 but also exhibited significant inhibition towards *h*-NPP3 and, therefore, was not selective. For the investigation of the binding interactions of potent inhibitor against *h*-NPP1, **6j** was selected. Molecular docking analyses were performed against all the lead derivatives in their respective proteins. Binding mode investigation of levamisole [(*S*)-6-phenyl-2,3,5,6-tetrahydroimidazo[2,1-*b*]thiazole] and potent compound **(6a)** within the active pocket of *h*-TNAP presented that His362, His437 and His324 were associated with π-π interactions by the phenyl of levamisole and 1,3-dimethylpyrimidinetrione ring of the compound. In addition, hydrogen bond interactions were noticed that may have profound impact on the inhibition potential. The H-bonding was noticed between basic residues and O atom of the trione moiety of **6a**. The amino acid residues intricate in making H-bonds were His321, Tyr170, Arg151, His434 and His154. Very interestingly, it was noticed that the interactions with metal ions which are important for the inhibitory activity were shown by carbonyl oxygen of **6a** and Zn ion and their bond distance was 2.28 Å. Similarly, phenyl group established contact with Zn ion with a bond distance of 3.76 Å. However, levamisole interacted with Zn ion by a bond distance of 3.72 Å. These metal interactions are supposed to form stable inhibitor-enzyme (EI) complex. The 3D binding interactions of levamisole and compound **6a** are shown in Fig. 5(a and b, respectively).

The investigation of the binding interactions of L-phenylalanine and the potent compound **6c** inside the active pocket of *h*-IAP revealed that the important amino acid residues taking part within the active pocket were Arg150, His153, His317, His320, Glu321 and Glu108. The π-π interactions were examined between aryl ring of phenylalanine and amino acid His320. Similar interactions were also noticed for compound **6c** and His320 and His317, when 3D diagrams were analyzed. His360 and Arg166 along with Tyr169 were intricate in H- bonding and these bindings are shown in Fig. 6(a and b). Within the active site of *h*-IAP, Mg^{+2} ions along with Zn^{+2} ions were present. Taking into account the interactions with metal ions, it was found that the bond distance between pyrimidine ring in compound **6c** and Zn^{+2} ion was 3.59 Å (Fig. 6b). Both the Zn^{+2} ions were playing active role in interactions with phenylalanine, first one at a distance of 2.86 Å, however, second at 4.09 Å (Fig. 6a), while Mg^{+2} ion was present at bond distance of 5.18 Å from oxygen atom of phenylalanine. Most of the interactions were shown by O atom of phenylalanine. On the other hand, the chlorine atom of the phenyl group in compound **6c** was directed towards the amino acid Arg150 and His153, and 1,3-dimethyl pyrimidinetrione

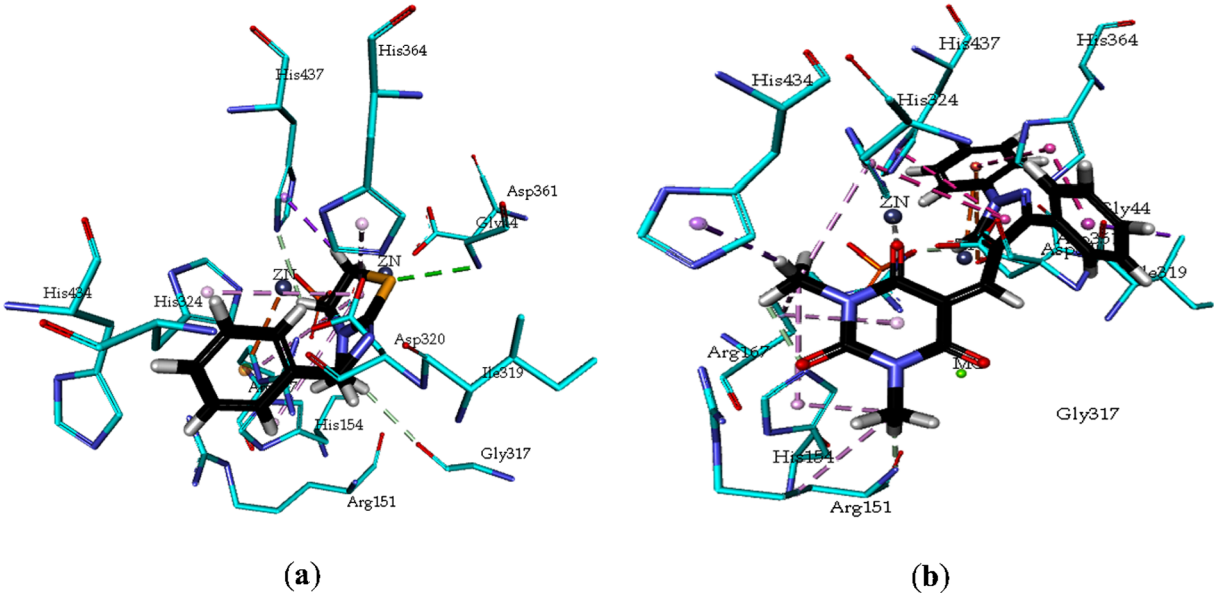

Fig. 5. Putative binding interactions of levamisole (a) and compound **6a** (b) within the active pocket of *h*-TNAP.

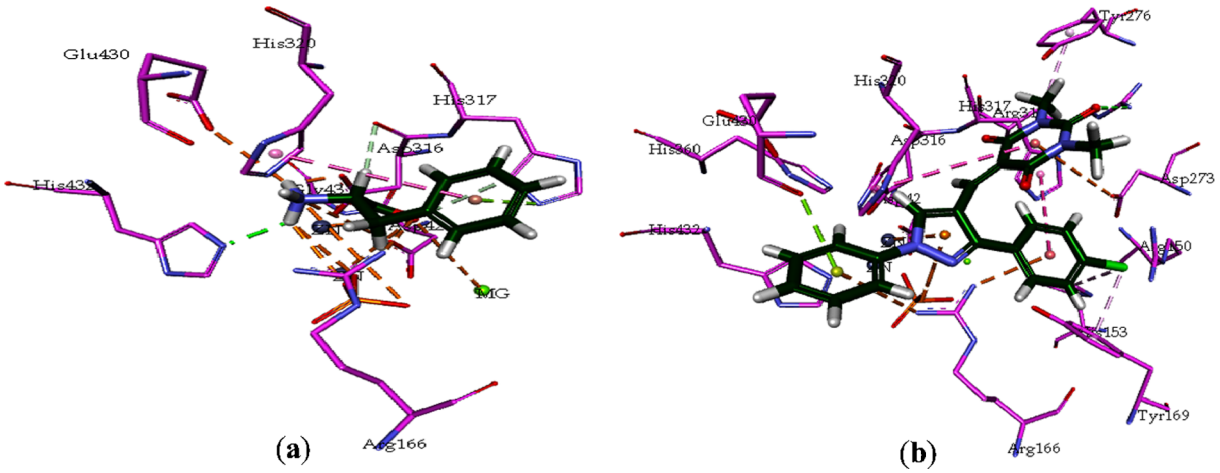

Fig. 6. Putative binding mode of L-phenylalanine (a) and compound **6c** (b) within the active pocket of *h*-IAP.

moiety was present in the middle of the active pocket where metal ions were positioned. The interactions and layout of compound **6c** against *h*-IAP may be the contributing factor for its higher inhibition activity.

When *h*-NPP1 was considered, the binding interactions were studied for suramin, the reference standard, and the potent compound (**6b**) from the tested series. However, the compound, **6j**, was found as most selective inhibitor of NPP1, therefore the docking studies were also carried out for this compound. The important amino acid residues taking part in the active site of *h*-NPP1 were Lys255, His535, His380, Thr256, Leu290 and Asp218 in addition to Zn^{+2} ions. The amino acid

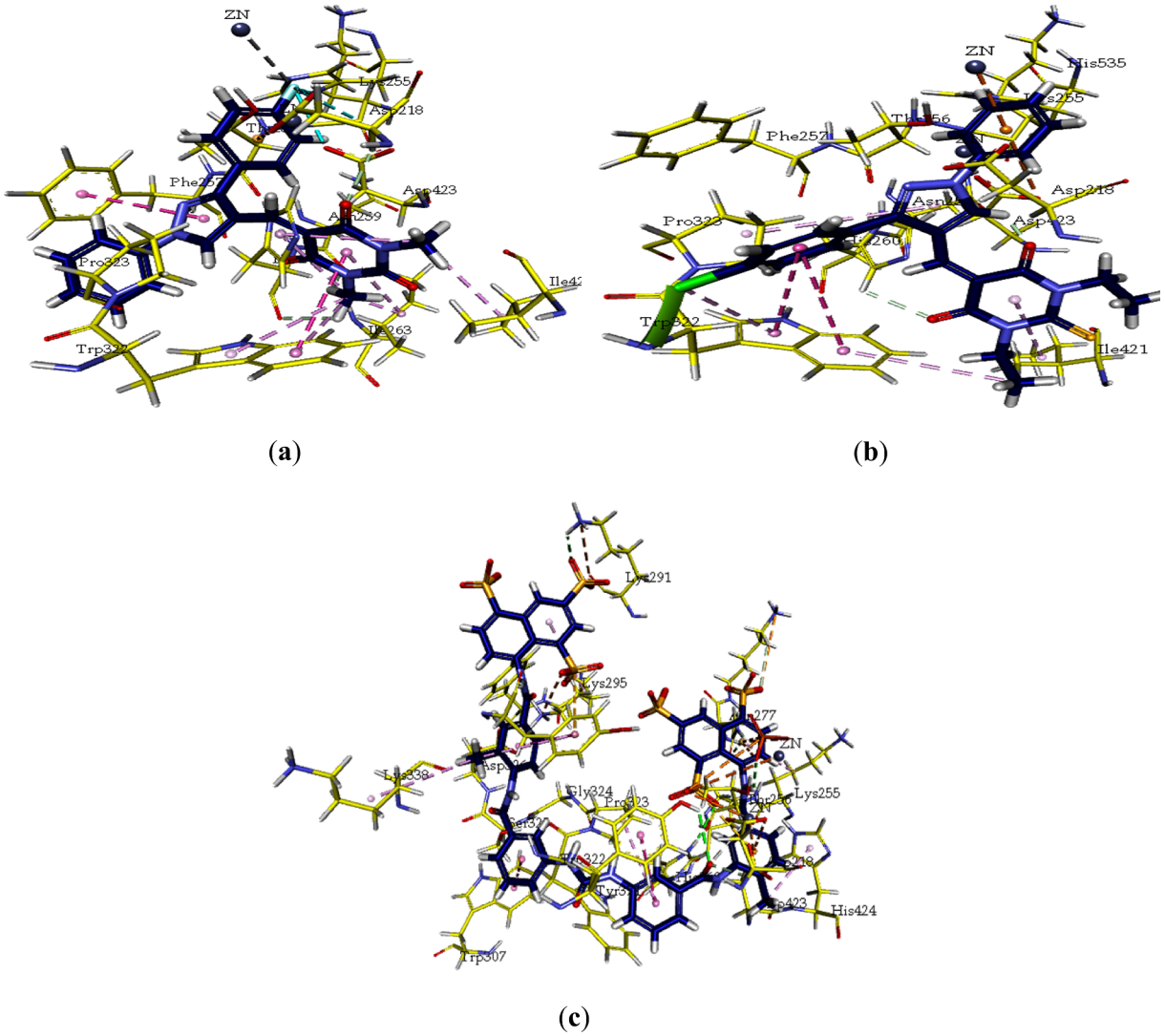

Fig. 7. Putative binding mode of compound **6b** (a), **6j** (b) and suramin (c) inside the active pocket of *h*-NPP1.

residues were important to exhibit the interactions with the compounds, **6b** and **6j**. In case of **6b**, it was observed that fluorophenyl group was oriented more towards Zn^{+2} ion in the active pocket and fluorine atom was at a bond distance of 3.57 Å. The oxygen atoms of suramin were showing interactions with Zn^{+2} ions at a bond distance of 5.41 Å and 3.66 Å. Suramin contained 4,6,8-trisulphonapthalen and 1,3,5-trisulfonic acid, the groups interacted in very good way with active site amino acids of *h*-NPP1 and interactions are shown in Fig. 7c. The π-π interactions were noticed among important residues and trisubstituted pyrazole moiety. Moreover, fluorophenyl part was involved in such interactions as well. Hydrogen bonding was noticed among basic amino acids of the active pocket of *h*-NPP1 and 2,4,6-pyrimidinetrione moiety of compound **6b** (Fig. 7a). When the docking results of **6j** were taken into account, the 4-chloro substituent attached to phenyl ring was found oriented towards Trp322 and making π-π interactions. Moreover, Ile421 was also involved in π-π interactions with 2-thioxodihydropyrimidine-4,6(1*H*,5*H*)-dione moiety. $Zinc^{+2}$ ion was noticed to show interactions with phenyl group of 1*H*-pyrazol-4-yl-5-methylene attached to 2-thioxodihydropyrimidine-4,6(1*H*,5*H*)-dione of compound **6j**. The interactions are presented in Fig. 7b.

For *h*-NPP3, the potent compound was **6h**, however, compound **6b** also showed significant inhibition. Therefore, the docking analysis were performed for both the inhibitors and binding poses and interactions were analyzed and compared with the binding shown by suramin inside the active pocket (Fig. 8). The observation of metal interactions showed that oxygen group of suramin was located at 5.37 Å bond distance, while oxygen atom of compound **6b** was at a distance of 4.88 Å from $Zinc^{+2}$ ion. However, phenyl ring of the potent compound was at a distance of 3.31 Å from Zn^{+2} ion. The strong metallic interaction may be possible justification for the potential inhibitory effect exhibited by compound **6h**. 3D binding mode investigation showed that compound **6h** was well-occupied within the active pocket of *h*-NPP3, resulting in strong H bonds. Another reason that may contribute towards the inhibitory profile of compound **6h** may be due to the presence of 1,3-diethyl group attached to 2-thioxodihydropyrimidine-4,6-(1*H*,5*H*)-dione functionality, as it was noticed that the moiety is showing interactions with most of the amino acids in active site of enzyme. Both the compounds, **6b** and **6h**, depicted strong hydrogen bonds in addition to π-π interactions with the important residues of *h*-NPP3 (Fig. 8). This type of binding interactions plays a vital role in the orientation of 3D coordinates of inhibitors/ligands within the active site and increase the stability/strength of enzyme-ligand complex, therefore, providing comprehensive structural insight of ligands within the active pocket of enzyme.

The details of ligand-proteins interactions, residues forming hydrogen bonding and π-π interactions within the active site of target proteins and their colors for all the docking interactions are provided in Table S1.

2.3.1. HYDE assessment of selective compounds

HYDE visual affinity was performed for the first 20 ranked docked conformers inside the active pocket of the homology models of human TNAP, IAP, NPP1 and NPP3 to depict the optimization of ligands. It correctly gives information for the ligand efficiency in addition to selectivity towards the most potent compound (Figs. S1–S4). The binding energy and docking score by FlexX for the selective derivatives are given in Table 2. The FlexX docking score presented that the potent compound has lower energy scores as compared to non-selective inhibitors. Moreover, the binding free energies ΔG showed that the potent inhibitors exhibited higher affinity towards their respective targets. Compound **6a** interacted with the *h*-TNAP in a very efficient manner in comparison to **6c** and gave favorable contributions. Similarly, **6c** showed higher affinity than **6a** towards *h*-IAP. The same trend was observed for the most potent inhibitors of *h*-NPP1 and *h*-NPP3, **6j** and **6h,** respectively. The selective compounds showed significant efficiency towards the protein as compared to other compounds.

2.4. Mechanism of inhibition

In order to explore the mode of inhibition, the kinetic studies were performed for compounds **6a**, **6c**, **6b** and **6h**, the most potent inhibitors of human TNAP, IAP, NPP1 and NPP3, respectively. The Lineweaver-Burk plot for compound **6a** revealed an un-competitive mode of inhibition, whereas compounds **6c**, **6b** and **6h** showed a competitive mode of inhibition by illustrating the same y-intercept for uninhibited and inhibited enzymes (Fig. 4). Furthermore, Michaelis-Menten kinetic parameters; K_m and V_{max} for *h*-TNAP, *h*-IAP, *h*-NPP1 and *h*-NPP3 inhibition were also determined in the presence and absence of inhibitor **6a**, **6c**, **6b** and **6d**, respectively. In case of **6c**, the maximal velocity ($V_{max)}$ was found in decreasing order at different concentrations of **6c**, whereas the Michaelis constant (K_m) was found almost constant (Fig. 4a). On the other hand, in case of compounds **6c**, **6b** and **6h**, the maximal velocity (V_{max}) was noted as constant although different concentrations of respective inhibitors were used, whereas, the Michaelis constant (K_m) was noticed to increase (Fig. 4b–d).

2.5. Anticancer activity

Anticancer activity in terms of cytotoxicity of pyrazolyl pyrimidinetrione and thioxopyrimidinedione derivatives (**6a–n**) against three different cancer cell lines, including breast cancer (MCF-7), myelogenous leukemia (K-562) and HeLa cell lines in comparison to normal cells (baby hamster kidney cell line; BHK-21) was determined using MTT assay. The cytotoxicity after 24 h treatment with 100 μM concentration of respective derivative was assessed in these experiments. Carboplatin was used as a standard drug. The obtained results are expressed as a percentage of growth inhibition with reference to untreated controlled cells and are presented in Table 3.

When pyrazolyl pyrimidinetriones/thioxopyrimidinediones **(6a–n)** were tested against normal cell lines (baby hamster kidey cell line; BHK-21), it was observed that PPT and PTP derivatives are less effective against normal cells showing low effect on growth reduction, hence can be good candidates as anticancer agents. When tested against cancer cell lines, it was observed that pyrazolyl pyrimidinetriones/thioxopyrimidinediones **(6a–n)** displayed promising anticancer activity in terms of cytotoxicity. With regard to MCF-7 cell lines, pyrazolyl pyrimidinetriones **(6a–g)** were found to have higher cytotoxic activity as compared to their thioxo analogs **(6h–n)**. Compounds **6a, 6b** and **6e** showed higher cytotoxicity than the rest of the candidates of the series. However, their cytotoxicity was relatively lower as compared to carboplatin. Intriguingly, compound **6b** (the most active inhibitor against NPP1) showed highest anticancer activity against breast cancer cell line. Anticancer activity with regard to chronic myelogenous leukemia cell lines (k-562) revealed that compounds **6a** and **6g** from PPTs and compounds **6i, 6j** and **6k** from PTPs displayed promising activity with reference to the standard. Interestingly, compound **6a** (the most active inhibitor against TNAP) showed promising activity against K-562 cells. Furthermore, a good cytotoxic profile was obtained when compounds were tested against HeLa cell lines exhibiting good to moderate activity. It was found that compound **6c** showed high % growth inhibition against Hela Cells. The most active anticancer compounds were pyrimidinetriones, **6a, 6c** and **6b** bearing H, F and Cl substituents on the phenyl ring of pyrazole moiety, causing 92, 82 and 85% reduction in the cell growth of K-562, HeLa and MCF-7, respectively, at 100 μM concentration (Fig. 9). It may be derived from the above discussion that the observed effects were dependent on the nature of substituent on aryl ring of pyrimidine nucleus.

These most active compounds were further selected for the determination of IC_{50} values against MCF-7, K-562 and HeLa cells (Table 4). The IC_{50} values showed that compound **6b** bearing pyrimidinetrione moiety and a fluoro substituent on the phenyl ring of pyrazole moiety possesses significantly higher cytotoxic activity towards MCF-7 cells. Similarly, compounds **6a** (bearing pyrimidinetrione

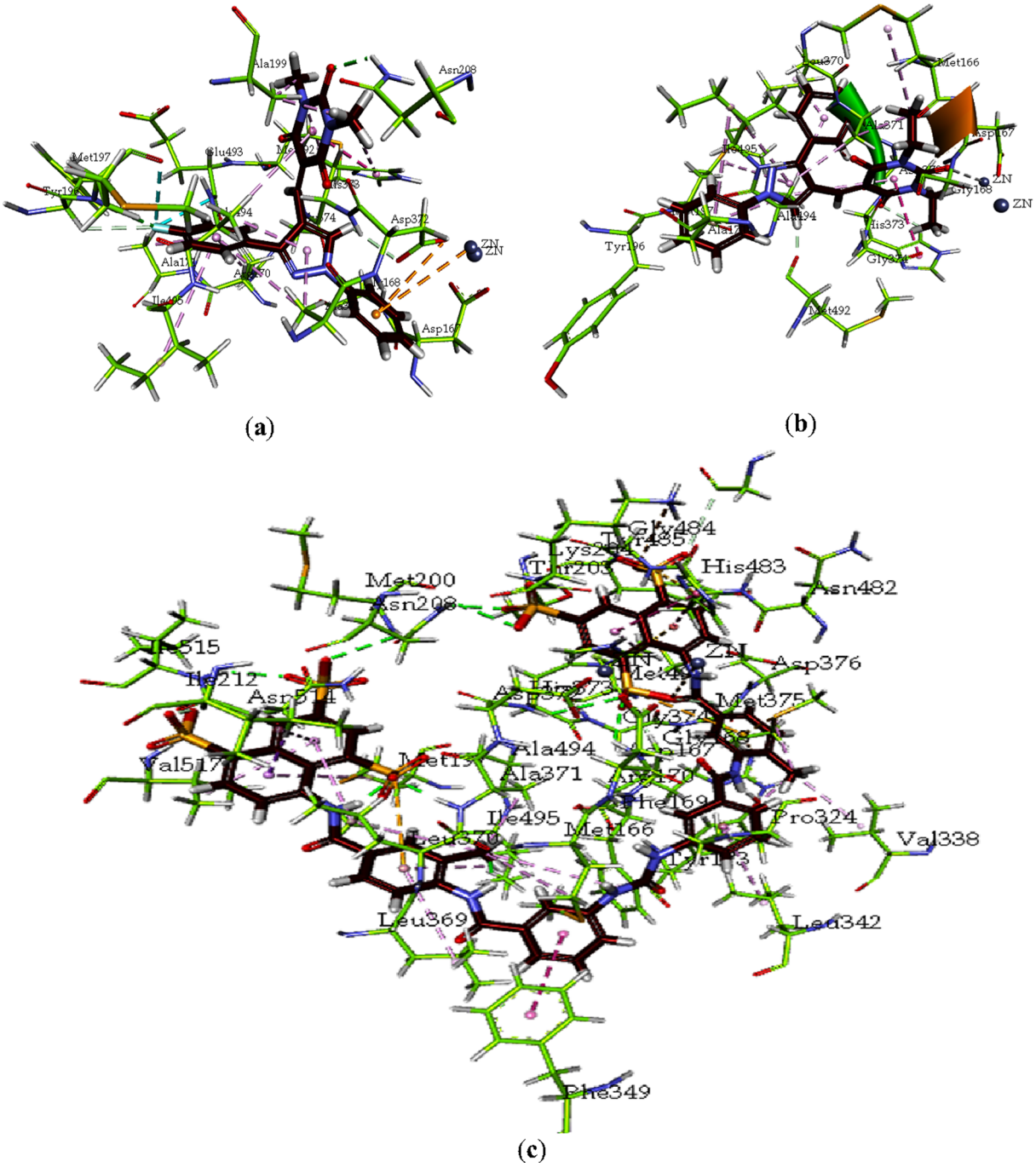

Fig. 8. Putative binding interactions of compound **6b** (a), compound **6 h** (b), and suramin (c) inside the active site of *h*-NPP3.

moiety and 1,3-diphenyl ring on pyrazole nucleus) exhibited maximum cytotoxic activity towards K-562, while compound **6c** (bearing 1-phenyl-3(4-chorophenyl moiety on pyrazolyl ring and a pyrimidinetrione nucleus) exhibited maximum cytotoxic activity against HeLa cells.

3. Conclusions

In summary, a pharmacophore integration methodology leading to a diverse range of pyrazole coupled pyrimidinetriones (**6a–g**) and thioxopyrimidinediones (**6h–n**) was successfully established. The synthesized derivatives were investigated for the inhibitory potency against human recombinant alkaline phosphatases (TNAP and IAP) and nucleotide pyrophosphatases (NPP1 and NPP3). *In vitro* biological assay results explicitly predicted the selective and potent inhibition of both target enzymes. Among the screened derivatives, compound **6a** caused the selective inhibition of *h*-TNAP with ~60-fold higher efficacy than the standard, whereas compound **6c** selectively inhibited *h*-IAP isozyme with IC_{50} value of 0.86 ± 0.04 μM. Most interestingly, compounds **6b** and **6h** appeared as lead scaffolds against *h*-NPP1 and *h*-NPP3 enzymes, respectively. The docking analysis revealed that these molecules establish hydrogen bonds as well as several other electrostatic interactions with important amino acid residues. The Lineweaver-Burk plot for potent compound **6a** demonstrated an un-competitive mode of inhibition, whereas compounds **6c**, **6b** and **6h** showed a competitive mode of inhibition. Moreover, compounds **6a**, **6b** and **6c** caused 92, 85 and 82% reduction in the cell growth of MCF-7, K-562 and HeLa cell lines, respectively, at 100 μM concentration. Collectively, the newly developed

Table 2
Ligand efficiency scores and the ranks after HYDE visual inspection.

Code	Docking score by FlexX for top pose	Free energy of bindingΔG (kJ mol^{-1})
h-TNAP		
6a	−18.36	−17
6c	−15.53	−9
h-IAP		
6a	−14.11	6
6c	−16.42	−4
h-NPP1		
6h	−18.42	−12
6j	−19.68	−17
h-NPP3		
6h	−20.58	−19
6j	−17.43	−11

Table 3
Cytotoxic effects of hybrid compounds (**6a–n**).

Compound	MCF-7	K-562	HeLa	BHK-21
	% inhibition ± SEM*			
6a	72.7 ± 2.41	92.2 ± 2.57	68.7 ± 2.16	13.8 ± 0.56
6b	85.4 ± 3.18	45.1 ± 1.25	77.1 ± 3.27	11.3 ± 0.37
6c	59.1 ± 1.44	19.6 ± 1.06	82.1 ± 3.68	15.7 ± 0.98
6d	62.7 ± 1.79	45.1 ± 1.54	72.4 ± 3.36	9.77 ± 0.45
6e	70.9 ± 1.64	27.5 ± 1.23	48.1 ± 2.46	16.4 ± 0.23
6f	61.1 ± 2.11	17.6 ± 0.78	11.1 ± 1.65	5.70 ± 0.17
6g	44.6 ± 1.21	86.3 ± 2.15	71.8 ± 3.26	8.45 ± 0.33
6h	57.1 ± 1.32	56.9 ± 1.56	73.6 ± 2.78	7.81 ± 0.78
6i	69.9 ± 2.49	84.3 ± 2.71	64.1 ± 1.68	10.1 ± 0.27
6j	51.2 ± 2.16	90.2 ± 3.26	61.4 ± 2.69	24.1 ± 0.89
6k	53.2 ± 1.33	83.2 ± 2.97	73.7 ± 1.79	27.6 ± 1.25
6l	50.7 ± 2.94	56.9 ± 0.77	69.5 ± 2.34	25.2 ± 2.56
6m	59.4 ± 2.68	68.6 ± 1.39	78.4 ± 3.88	14.9 ± 0.89
6n	58.7 ± 1.82	31.4 ± 0.78	66.7 ± 1.78	12.6 ± 0.65
Carboplatin	90.7 ± 1.26	82.8 ± 1.78	85.2 ± 1.57	18.4 ± 0.45

* The percentage of growth inhibition was expressed in relation to untreated control cells as Means ± SEM values.

hybrid structural scaffolds provide a valuable platform for the enhancement in the activity profile and to generate lead molecules for drug discovery.

4. Experimental section

4.1. Substrates and reagents

The acetophenones and glacial acetic acid were obtained from Sigma-Aldrich (Steinheim, Germany). Ethylenediamine was purchased from Merck (Darmstadt, Germany). The reagents used were of analytical grade. Ethanol, chloroform and methanol were provided by Lab Scan (Patuman, Bangkok). Ethyl acetate was the product of Riedel de Haen (Seezle, Germany). All solvents used were dried under nitrogen pressure by passage through activated alumina columns.

4.2. Instrumentation

Thin layer chromatography (TLC) was performed on Merck 0.2 mm DF $60F_{254}$ precoated aluminium plates. The compounds were visualized by exposure to UV light at 254 nm. Melting points were recorded using Gallenkamp melting point apparatus (MP-D) in open capillaries and are uncorrected. FTIR spectra were recorded using attenuated total reflectance (ATR) facility on a Thermoscientific Fourier Transform Infra-Red Spectrophotometer (USA) model nicolet 6700. The elemental analysis was performed using Leco CHNS-932 Elemental Analyzer (USA). NMR spectra were acquired on Bruker DQX400 at room temperature. ^{1}H and ^{13}C NMR spectra were referenced to tetramethylsilane *via* the residual protonated solvent (^{1}H) or the solvent itself (^{13}C). All chemical shifts are reported in parts per million (ppm). For $CDCl_3$, the shifts are referenced to 7.26 ppm for ^{1}H NMR spectroscopy and 77.16 ppm for ^{13}C NMR spectroscopy. High-resolution mass spectra were recorded on a Micromass LCT electrospray ionization mass spectrometer operating at a resolution of 5000 full width half height.

4.3. General procedure for the synthesis of phenyl-3-aryl-1H-pyrazole-4-carbaldehydes (4a–g)

Synthesis of phenyl-3-aryl-1*H*-pyrazole-4-carbaldehydes **(4a–g)** reported in our previous work [29]. To a stirred solution of phenyl hydrazine **1** (12 mmol, 1.29 g or 1.18 mL) in absolute ethanol (20 mL) was added acetophenone **2** (10 mmol) and glacial acetic acid (0.3 mL). The reaction mixture was kept on stirring at 70 °C. After completion of the reaction (as monitored by TLC), the excess solvent was evaporated to yield crude solid, which was filtered, washed with cold ethanol, dried and recrystallized from ethanol to yield the corresponding hydrazone (**3**).

The appropriate acetophenone phenyl hydrazone (1.0 mmol) was added to a cold solution of dimethylformamide (DMF) (4 mL) and phosphorus oxychloride (0.5 g, 3.0 mmol) and the resulting mixture heated at 70 °C for 3 h. The mixture was cooled to room temperature and poured onto crushed ice, neutralized with an aqueous solution of sodium hydroxide (for compounds **4a**, **4e** and **4f**) or sodium hydrogen carbonate (for compounds **4b–d** and **4g**). The precipitated solid was filtered and purified by flash column chromatography (20% EtOAc in *n*-hexane) in case of compounds **4a**, **4e** and **4f**, while recrystallized from ethanol to afford the rest of pyrazole-4-carbaldehydes (**4b–d** and **4g**).

4.4. General procedure for the synthesis of 1-phenyl-3-arylpyrazol-4-yl-5-methylene-N,N'-dialkylpyrimidine-2,4,6-triones (PPTs) (6a–g) and 1-phenyl-3-arylpyrazol-4-yl-5-methylene-N,N'-dialkyl-2-thioxopyrimidine-4,6-diones (PTPs) (6h–n)

To a stirred solution of 1,3-dimethylpyrimidine-2,4,6(*1H,3H,5H*)-trione or 1,3-dimethyl-2-thioxodihydropyrimidine-4,6-dione (1.0 mmol) in chloroform/methanol (8:1; 20 mL), glacial acetic acid (2 mmol) was added followed by ethylenediamine (0.2 mmol). The resulting mixture was stirred for 15 min followed by the addition of 3-(4-substituted phenyl)-1-phenyl-1*H*-pyrazole-4-carbaldehyde **(4a–g)** (1.2 mmol) at ambient temperature. After completion of the reaction (TLC; 30% acetone in *n*-hexane), excess solvent was removed *in vacuo* to afford a bright yellow solid. The crude solid was washed with water, dried and recrystallized (chloroform/ethanol) to yield the desired compounds **(6a–n)**.

4.4.1. 4.4.1. 5-((1,3-Diphenyl-1H-pyrazol-4-yl)methylene)-1,3-dimethylpyrimidine-2,4,6-(1H,3H,5H)trione **(6a)**

Pale yellow solid (84%); m.p.: 198–200 °C; R_f: 0.42 (30% acetone in *n*-hexane); FTIR (ATR, cm^{-1}): 3025 (=C−H), 2944, 2813 (2× C−H), 1690 (C=O), 1564 (C=N), 1570, 1513 (2× C=C); ^{1}H NMR (400 MHz, Chloroform-*d*): δ 9.83 (1H, s, $C-H_{pyrazolyl}$), 8.28 (1H, s, $=C-H_{olefinic}$), 8.00–7.92 (2H, m, Ar-H), 7.62 (7H, m, Ar-H), 7.54–7.46 (1H, m, Ar-H), 3.28 (3H, s, CH_3), 3.22 (3H, s, CH_3); ^{13}C NMR (101 MHz, Chloroform-*d*): δ 162.79 (C=O), 161.75 (C=O), 158.61 (C=O), 151.53, 144.88, 138.97, 134.84, 131.17, 130.41, 129.99, 129.92, 129.40, 128.61, 120.16, 115.72, 114.55, 29.00 (CH_3), 28.43 (CH_3); HRMS (ESI + ve) exact mass calculated for $C_{22}H_{18}N_4O_3$ $[M+H]^+$: 386.4001; Found: 386.4006; Analysis calculated: C 68.38, H 4.70, N 14.50; Found: C 68.45, H 4.74, N 15.43.

4.4.2. 4.4.2. 5-((3-(4-Fluorophenyl)-1-phenyl-1H-pyrazol-4-yl)methylene)-1,3-dimethylpyrimidine-2,4,6-(1H,3H,5H)-trione **(6b)**

Pale yellow solid (89%); m.p.: 202–204 °C; R_f: 0.49 (30% acetone in

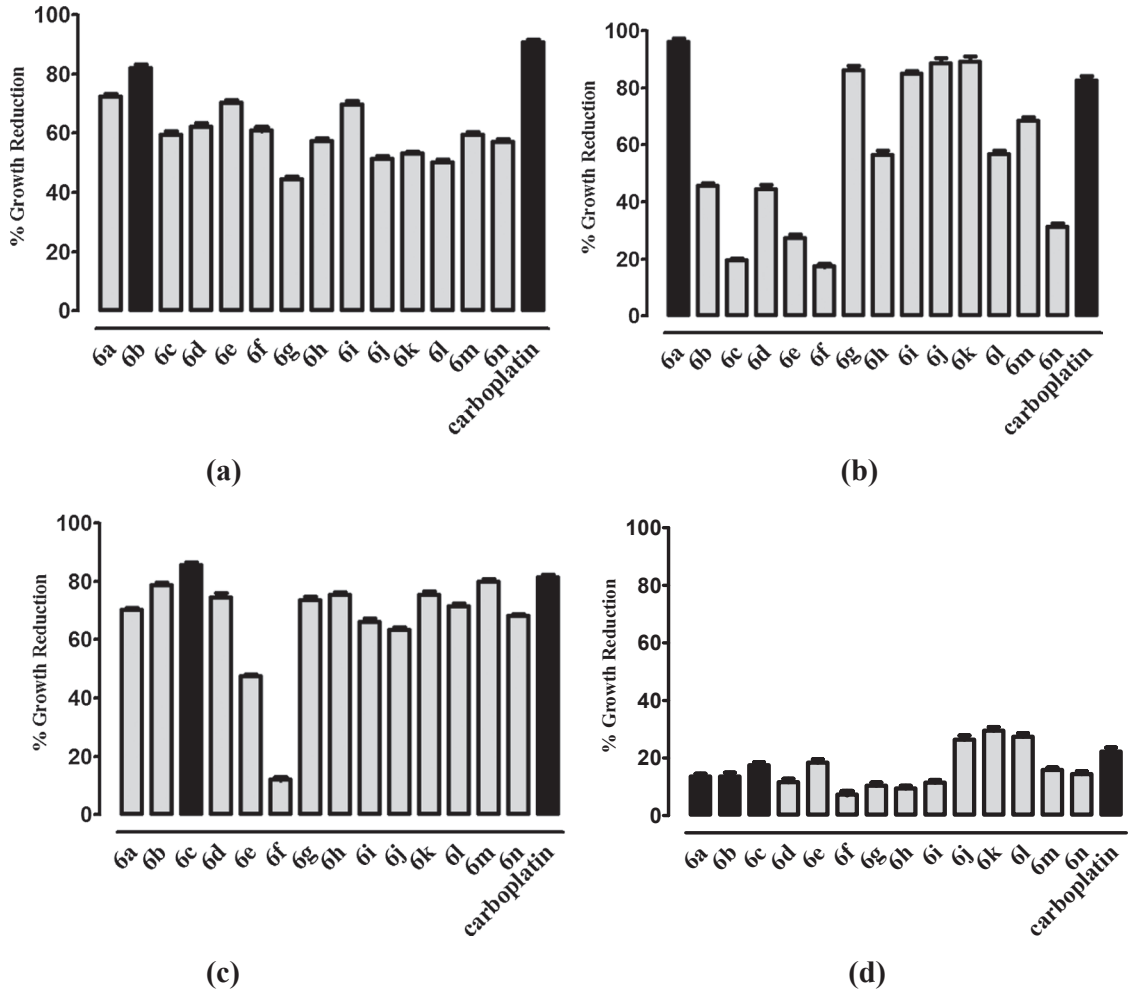

Fig. 9. . Cytotoxic potential of compounds **6a–n** against MCF-7 (a); K-562 (b); HeLa in comparison to normal cells (c); and BHK-21 cells (d). Cytotoxicity was quantified spectrophotometrically using an MTT assay.

Table 4
Cytotoxic effect of the most potent compounds (**6a–c**) on different cell lines.

Compound	MCF-7	K-562	HeLa
	IC_{50} ± SEM*		
6b	1.35 ± 0.03	> 100	8.41 ± 0.89
6a	4.78 ± 0.66	1.66 ± 0.01	7.09 ± 0.77
6c	5.11 ± 0.67	> 100	1.24 ± 0.04
Carboplatin	3.91 ± 0.32	1.8 ± 0.78	5.13 ± 0.45

* IC_{50} denotes compound concentrations that result in a 50% decrease in the cell number compared to non-treated controls and were derived from 24 h treatment. Results from three independent experiments are presented.

n-hexane); FTIR (ATR, cm^{-1}): 3014 (=C−H), 2940, 2811 (2× C−H), 1662 (C=O), 1563 (C=N), 1569, 1507 (2× C=C); ^{1}H NMR (400 MHz, Chloroform-*d*): δ 9.81 (1H, s, C−$H_{pyrazolyl}$), 8.48 (1H, s, =C−$H_{olefinic}$), 7.87–7.79 (2H, m, Ar-H), 7.60–7.52 (2H, m, Ar-H), 7.51–7.42 (2H, m, Ar-H), 7.39–7.30 (1H, m, Ar-H), 7.22–7.13 (2H, m, Ar-H), 3.37 (3H, s, CH_3), 3.33 (3H, s, CH_3); ^{13}C NMR (101 MHz, Chloroform-*d*): δ 165.79 (C=O), 164.61 (C=O), 163.07 (C=O), 159.41 (d, ^1J = 249.4 Hz, C-F), 149.80, 147.52, 135.08, 131.61, 131.53, 129.67, 128.19, 121.34, 120.08, 116.22, 116.01, 28.92 (CH_3), 28.27 (CH_3); HRMS (ESI + ve) exact mass calculated for $C_{22}H_{17}FN_4O_3$ $[M+H]^+$: 404.3918; Found: 404.3918; Analysis calculated: C 65.34; H 4.24, N 13.85; Found: C 65.39, H 4.27, N 13.90.

4.4.3. 4.4.3. 5-((3-(4-Chlorophenyl)-1-phenyl-1H-pyrazol-4-yl)methylene)-1,3-dimethylpyrimidine-2,4,6-(1H,3H,5H)-trione ***(6c)***

Brownish orange solid (80%); m.p.: 197–199 °C; R_f: 0.52 (30% acetone in *n*-hexane); FTIR (ATR, cm^{-1}): 3016 (=C−H), 2933, 2843 (2× C−H), 1695 (C=O), 1617 (C=N), 1563, 1511 (2× C=C); ^{1}H NMR (400 MHz, Chloroform-*d*): δ 9.88 (1H, s, C−$H_{pyrazolyl}$), 8.54 (1H, s, =C−$H_{olefinic}$), 7.93–7.86 (2H, m, Ar-H), 7.67–7.58 (2H, m, Ar-H), 7.58–7.49 (2H, m, Ar-H), 7.46–7.37 (1H, m, Ar-H), 7.29–7.19 (2H, m, Ar-H), 3.44 (3H, s, CH_3), 3.40 (3H, s, CH_3); ^{13}C NMR (101 MHz, Chloroform-*d*): δ 163.54 (C=O), 162.37 (C=O), 159.12(C=O), 152.13, 147.98, 139.69, 135.87, 132.94, 131.94, 130.61, 130.43, 128.99, 124.87, 120.81, 116.69, 113.65, 29.68 (CH_3), 29.03 (CH_3); HRMS (ESI + ve) exact mass calculated for $C_{22}H_{17}ClN_4O_3$ $[M+H]^+$: 420.8484; Found: 420.8489; Analysis calculated: C 62.79, H 8.42, N 13.31; Found: C 62.85, H 4.10, N 13.28.

4.4.4. 4.4.4. 5-((3-(4-Bromophenyl)-1-phenyl-1H-pyrazol-4-yl)methylene)-1,3-dimethylpyrimidine-2,4,6-(1H,3H,5H)-trione ***(6d)***

Pale yellow solid (88%); m.p.: 210–212 °C; R_f: 0.62 (30% acetone in *n*-hexane); FTIR (ATR, cm^{-1}): 3018 (=C−H), 2924, 2813 (2× C−H), 1680 (C=O), 1610 (C=N), 1565, 1512 (2× C=C); ^{1}H NMR (400 MHz, Chloroform-*d*): δ 9.80 (1H, s, C−$H_{pyrazolyl}$), 8.45 (1H, s, =C−$H_{olefinic}$), 7.88–7.77 (2H, m, Ar-H), 7.65–7.57 (2H, m, Ar-H), 7.51–7.40 (4H, m, Ar-H), 7.39–7.30 (1H, m, Ar-H), 3.36 (3H, s, CH_3) 3.32 (3H, s, CH_3); ^{13}C NMR (101 MHz, Chloroform-*d*): δ 162.79 (C=O), 161.62 (C=O), 158.36 (C=O), 151.38, 147.23, 138.93, 135.12, 132.19, 131.19,

129.85, 129.68, 128.23, 124.11, 120.05, 115.93, 112.89, 28.93 (CH_3), 28.28 (CH_3); HRMS (ESI + ve) exact mass calculated for $C_{22}H_{17}BrN_4O_3$ $[M+H]^+$: 465.2911; Found: 465.2914; Analysis calculated: C 56.79, H 3.68, N 12.04; Found: C 56.83, H 3.74, N 12.09.

4.4.5. 4.4.5. 1,3-Dimethyl-5-((1-phenyl-3-p-tolyl-1H-pyrazol-4-yl)methylene) pyrimidine-2,4,6- (1H,3H,5H)-trione ***(6e)***

Pale yellow solid (82%); m.p.: 223–225 °C; R_f: 0.66 (30% acetone in *n*-hexane); IR (ATR, cm^{-1}): 3019 (=C−H), 2938, 2809 (2× C−H), 1699 (C=O), 1602 (C=N), 1578, 1523 (2× C=C); ^{1}H NMR (400 MHz, Chloroform-*d*): δ 9.70 (1H, s, C−$H_{pyrazolyl}$), 8.53 (1H, s, =C−$H_{olefinic}$), 7.87–7.79 (2H, m, Ar-H), 7.49–7.40 (4H, m, Ar-H), 7.37–7.24 (3H, m, Ar-H), 3.35 (3H, s, CH_3), 3.32 (3H, s, CH_3), 2.36 (3H, s, CH_3); ^{13}C NMR (101 MHz, Chloroform-*d*): δ 162.91 (C=O), 161.73 (C=O), 159.77 (C=O), 151.48, 148.21, 139.52, 139.07, 134.99, 129.66, 129.61, 124.30, 128.03, 127.93, 120.06, 116.12, 112.38, 28.88 (CH_3), 28.24 (CH_3), 21.40 (CH_3); HRMS (ESI + ve) exact mass calculated for $C_{23}H_{20}N_4O_3$ $[M+H]^+$: 400.4207; Found: 400.4202; Analysis calculated: C 68.99, H 5.03, N 13.99; Found: C 69.10, H 5.09, N 13.92.

4.4.6. 4.4.6. 5-((3-(4-Methoxyphenyl)-1-phenyl-1H-pyrazol-4-yl)methylene)-1,3-dimethylpyrimidine-2,4,6-(1H,3H,5H)-trione ***(6f)***

Bright yellow solid (89%); m.p.: 215–217 °C; R_f: 0.68 (30% acetone in *n*-hexane); FTIR (ATR, cm^{-1}): 3020 (=C−H), 2949, 2816 (2× C−H), 1685 (C=O), 1620 (C=N), 1574, 1538 (2× C=C); ^{1}H NMR (400 MHz, Chloroform-*d*): δ 9.80 (1H, s, C−$H_{pyrazolyl}$), 8.54 (1H, s, =C-$H_{olefinic}$), 7.87–7.79 (2H, m, Ar-H), 7.56–7.41 (4H, m, Ar-H), 7.38–7.29 (1H, m, Ar-H), 7.04–6.96 (2H, m, Ar-H), 3.81 (3H, s, OCH_3), 3.36 (3H, s, CH_3), 3.34 (3H, s, CH_3); ^{13}C NMR (101 MHz, Chloroform-*d*): δ 162.97 (C=O), 160.74 (C=O), 159.67 (C=O), 148.26, 139.07, 135.01, 132.67, 131.03, 129.61, 128.04, 123.27, 124.55, 120.07, 116.07, 114.50, 113.45, 55.40 (OCH_3), 28.90 (CH_3), 28.25 (CH_3). HRMS (ESI + ve) exact mass calculated for $C_{23}H_{20}N_4O_4$ $[M+H]^+$: 416.4263; Found: 416.4263; Analysis calculated: C 66.34, H 4.84, N 13.45; Found: C 66.39, H 4.87, N 13.50.

4.4.7. 4.4.7. 1,3-Dimethyl-5-((3-(4-nitrophenyl)-1-phenyl-1H-pyrazol-4-yl)methylene)pyramidine-2,4,6-(1H,3H,5H)-trione ***(6g)***

Pale yellow solid (90%): m.p.: 227–229 °C; R_f: 0.61 (30% acetone in *n*-hexane); FTIR (ATR, cm^{-1}): 3020 (=C−H), 2940, 2825 (2× C−H), 1689 (C=O), 1623 (C=N), 1576, 1516 (2× C=C); ^{1}H NMR (400 MHz, Chloroform-*d*): δ 9.87 (1H, s, C−$H_{pyrazolyl}$), 8.52 (1H, s, =C−$H_{olefinic}$), 7.95–7.84 (2H, m, Ar-H), 7.72–7.64 (2H, m, Ar-H), 7.58–7.47 (4H, m, Ar-H), 7.46–7.37 (1H, m, Ar-H), 3.42 (3H, s, CH_3) 3.41 (3H, s, CH_3); ^{13}C NMR (101 MHz, Chloroform-*d*): δ 164.23 (C=O), 163.06 (C=O), 159.80 (C=O), 152.82, 148.67, 140.37, 136.56, 133.63, 132.63, 131.29, 131.12, 129.67, 125.55, 121.50, 117.37, 114.34, 30.37 (CH_3), 29.72 (CH_3); HRMS (ESI + ve) exact mass calculated for $C_{22}H_{17}N_5O_5$ $[M+H]^+$: 431.4011; Found: 431.4015; Analysis calculated: C 61.25, H 3.97, N 16.23; Found: C 61.31, H 4.03, N 16.21.

4.4.8. 4.4.8. 5-((1,3-Diphenyl-1H-pyrazol-4-yl)methylene)-1,3-diethyl-2-thioxodihydropyrimidine-4,6-(1H,5H)-dione ***(6h)***

Bright yellow solid (89%); m.p.: 193–195 °C; R_f: 0.62 (30% acetone in *n*-hexane); FTIR (ATR, cm^{-1}): 3011 (=C−H), 2938, 2811 (2× C−H), 1699 (C=O), 1616 (C=N), 1578, 1509 (2× C=C); ^{1}H NMR (400 MHz, Chloroform-*d*): δ 9.86 (1H, s, C−$H_{pyrazolyl}$), 8.54 (1H, s, =C−$H_{olefinic}$), 7.88–7.80 (2H, m, Ar-H), 7.61–7.53 (2H, m, Ar-H), 7.52–7.41 (5H, m, Ar-H), 7.41–7.29 (1H, m, Ar-H), 4.46 (2H, q, J = 7.0 Hz, CH_2), 4.53 (2H, q, J = 7.0 Hz, CH_2), 1.30 (3H, t, J = 7.0 Hz, CH_3), 1.22 (3H, t, J = 7.0 Hz, CH_3); ^{13}C NMR (101 MHz, Chloroform-*d*): δ 178.50 (C=S), 160.78 (C=O), 159.51 (C=O), 159.20, 148.84, 138.63, 134.89, 130.45, 129.43, 129.31, 129.20, 128.64, 127.86, 119.81, 116.35, 113.03, 43.71 (CH_2), 43.00 (CH_2), 12.19 (CH_3), 12.04 (CH_3); HRMS (ESI + ve) exact mass calculated for $C_{24}H_{22}N_4O_2S$ $[M+H]^+$: 430.5228; Found: 430.5223; Analysis calculated: C 66.96, H 5.15, N 13.01, S 7.45; Found: C 66.91, H 5.19, N 13.08, S 7.52.

4.4.9. 4.4.9. 1,3-Diethyl-5-((3-(4-fluorophenyl)-1-phenyl-1H-pyrazol-4-yl)methylene)-2-thioxodihydropyrimidine-4,6-(1H,5H)-dione ***(6i)***

Bright yellow solid (83%); m.p.: 216–218 °C; R_f: 0.67 (30% acetone in *n*-hexane); FTIR (ATR, cm^{-1}): 3018 (=C−H), 2939, 2813 (2× C−H), 1691 (C=O), 1615 (C=N), 1569, 1511 (2× C=C); ^{1}H NMR (400 MHz, Chloroform-*d*): δ 9.80 (1H, s, C−$H_{pyrazolyl}$), 8.45 (1H, s, =C−$H_{olefinic}$), 7.88–7.77 (2H, m, Ar-H), 7.65–7.57 (2H, m, Ar-H), 7.51–7.40 (4H, m, Ar-H), 7.39–7.30 (1H, m, Ar-H), 4.54 (2H, q, J = 7.1 Hz, CH_2), 4.47 (2H, q, J = 7.1 Hz, CH_2), 1.28 (3H, t, J = 7.1 Hz, CH_3), 1.22 (3H, t, J = 7.0 Hz, CH_3); ^{13}C NMR (101 MHz, Chloroform-*d*): δ 179.81 (C=S), 165.90 (C=O), 163.48 (C=O), 158.81 (d, ^1J = 242.4 Hz, C-F), 138.71, 134.97, 130.53, 129.39, 129.28, 128.72, 127.94, 124.60, 119.89, 116.43, 113.11, 43.79 (CH_2), 43.08 (CH_2), 12.27 (CH_3), 12.12 (CH_3); HRMS (ESI + ve) exact mass calculated for $C_{24}H_{21}FN_4O_2S$ $[M+H]^+$: 448.5124; Found: 448.5120; Analysis calculated: C 64.27, H 4.72, N 12.49, S 7.15; Found: C 64.43, H 4.69, N 12.49, S 7.18.

4.4.10. 4.4.10. 5-((3-(4-Chlorophenyl)-1-phenyl-1H-pyrazol-4-yl)methylene)-1,3-diethyl-2-thioxodihydropyrimidine-4,6-(1H,5H)-dione ***(6j)***

Orange solid (81%); m.p.: 189–191 °C; R_f: 0.72 (30% acetone in *n*-hexane); FTIR (ATR, cm^{-1}): 3011 (=C−H), 2934, 2803 (2× C−H), 1696 (C=O), 1612 (C=N), 1568, 1519 (2× C=C); ^{1}H NMR (400 MHz, Chloroform-*d*): δ 9.94 (1H, s, C−$H_{pyrazolyl}$), 8.62 (1H, s, =C−$H_{olefinic}$), 7.96–7.88 (2H, m, Ar-H), 7.69–7.61 (2H, m, Ar-H), 7.56–7.37 (5H, m, Ar-H), 4.62 (2H, q, J = 7.2 Hz, CH_2), 4.55 (2H, q, J = 7.2 Hz, CH_2), 1.36 (3H, t, J = 7.2 Hz, CH_3), 1.30 (3H, t, J = 7.2 Hz, CH_3); ^{13}C NMR (101 MHz, Chloroform-*d*): δ 179.04 (C=S), 161.32 (C=O), 160.05 (C=O), 159.75, 149.39, 139.18, 135.43, 131.00, 129.85, 129.74, 129.18, 128.41, 121.80, 120.35, 116.90, 113.58, 44.26 (CH_2), 43.55 (CH_2), 12.73 (CH_3), 12.59 (CH_3); HRMS (ESI + ve) exact mass calculated for $C_{24}H_{21}ClN_4O_2S$ $[M+H]^+$: 464.9674; Found: 464.9674; Analysis calculated: C 62.00, H 4.55, N 12.05, S 6.90; Found: C 62.11, H 4.59, N 12.12, S 6.87.

4.4.11. 4.4.11. 5-((3-(4-Bromophenyl)-1-phenyl-1H-pyrazol-4-yl)methylene)-1,3-diethyl-2-thioxodihydropyrimidine-4,6-(1H,5H)-dione ***(6k)***

Bright orange solid (81%); m.p.: 198–200 °C; R_f: 0.52 (30% acetone in *n*-hexane); FTIR (ATR, cm^{-1}): 3018 (=C−H), 2939, 2813 (2× C−H), 1698 (C=O), 1611 (C=N), 1588, 1515 (2× C=C); ^{1}H NMR (400 MHz, Chloroform-*d*): δ 9.95 (1H, s, C−$H_{pyrazolyl}$), 8.63 (1H, s, =C−$H_{olefinic}$), 7.97–7.89 (2H, m, Ar-H), 7.70–7.62 (2H, m, Ar-H), 7.57–7.51 (4H, m, Ar-H), 7.50–7.38 (1H, m, Ar-H), 4.63 (2H, q, J = 7.0 Hz, CH_2), 4.54 (2H, q, J = 7.0 Hz, CH_2), 1.37 (3H, t, J = 7.0 Hz, CH_3), 1.31 (3H, t, J = 7.0 Hz, CH_3); ^{13}C NMR (101 MHz, Chloroform-*d*): δ 178.97 (C=S), 161.25 (C=O), 159.98 (C=O), 159.67, 149.31, 139.10, 135.36, 130.93, 129.78, 129.67, 129.11, 128.33, 121.46, 120.28, 116.83, 113.51, 44.18 (CH_2), 43.48 (CH_2), 12.66 (CH_3), 12.51 (CH_3); HRMS (ESI + ve) exact mass calculated for $C_{24}H_{21}BrN_4O_2S$ $[M+H]^+$: 509.4182; Found: 509.4186; Analysis calculated: C 56.59, H 4.16, N 11.00, S 6.29; Found: C 56.53, H 4.21, N 11.07, S 6.33.

4.4.12. 4.4.12. 1,3-Diethyl-5-((1-phenyl-3-p-tolyl-1H-pyrazol-4-yl) methylene)-2-thioxodihydropyrimidine-4,6-(1H,5H)-dione ***(6l)***

Bright yellow solid (91%); m.p.: 223–225 °C; R_f: 0.72 (30% acetone in *n*-hexane); FTIR (ATR, cm^{-1}): 3015 (=C−H), 2944, 2813 (2× C−H), 1693 (C=O), 1610 (C=N), 1569, 1511 (2× C=C); ^{1}H NMR (400 MHz, Chloroform-*d*): δ 9.87 (1H, s, C−$H_{pyrazolyl}$), 8.55 (1H, s, =C−$H_{olefinic}$), 7.89–7.81 (2H, m, Ar-H), 7.62–7.54 (2H, m, Ar-H), 7.49–7.30 (5H, m, Ar-H), 4.53 (2H, q, J = 6.9 Hz, CH_2), 4.48 (2H, q, J = 6.9 Hz, CH_2), 2.36 (3H, s, CH_3) 1.27 (3H, t, J = 6.9 Hz, CH_3), 1.23 (3H, t, J = 6.9 Hz, CH_3); ^{13}C NMR (101 MHz, Chloroform-*d*): δ 178.45 (C=S), 160.74 (C=O), 159.46 (C=O), 159.16, 148.80, 138.59, 134.85, 131.44, 130.41, 129.27, 129.16, 128.60, 127.82, 119.77,

116.31, 112.99, 43.67 (CH_2), 42.96 (CH_2), 21.40 (CH_3), 12.15 (CH_3), 12.00 (CH_3); HRMS (ESI + ve) exact mass calculated for $C_{25}H_{24}N_4O_2S$ $[M+H]^+$: 444.5413; Found: 444.5410; Analysis calculated: C 67.54, H 5.44, N 12.60, S 7.21; Found: C 67.59, H 5.50, N 12.57, S 7.19.

4.4.13. 4.4.13. 1,3-Diethyl-5-((3-(4-methoxyphenyl)-1-phenyl-1H-pyrazol-4-yl)methylene)-2-thioxodihydro pyrimidine-4,6-(1H,5H)-dione **(6m)**

Bright yellow solid (86%); m.p.: 219–221 °C; R_f: 0.64 (30% acetone in *n*-hexane); FTIR (ATR, cm^{-1}): 3018 (=C−H), 2944, 2800 (2× C−H), 1691 (C=O), 1619 (C=N), 1562, 1514 (2× C=C); ^{1}H NMR (400 MHz, Chloroform-*d*): δ 9.84 (1H, s, C−$H_{pyrazolyl}$), 8.52 (1H, s, =C−$H_{olefinic}$), 7.86–7.78 (2H, m, Ar-H), 7.59–7.51 (2H, m, Ar-H), 7.46–7.40 (4H, m, Ar-H), 7.39–7.27 (1H, m, Ar-H), 4.54 (2H, q, J = 6.8 Hz, CH_2), 4.45 (2H, q, J = 6.8 Hz, CH_2), 3.81 (3H, s, OCH_3), 1.26 (3H, t, J = 6.8 Hz, CH_3), 1.20 (3H, t, J = 6.8 Hz, CH_3); ^{13}C NMR (101 MHz, Chloroform-*d*): δ 178.73 (C=S), 161.01 (C=O), 159.74 (C=O), 159.43, 149.07, 138.86, 135.12, 130.69, 129.54, 129.43, 128.87, 128.09, 121.54, 120.04, 116.59, 113.27, 55.40 (OCH_3), 43.94 (CH_2), 43.24 (CH_2), 12.42 (CH_3), 12.27 (CH_3); HRMS (ESI + ve) exact mass calculated for $C_{25}H_{24}N_4O_3S$ $[M+H]^+$: 460.5480; Found: 460.5485; Analysis calculated: C 65.20, H 5.25, N 10.42, S 6.96; Found: C 65.27, H 5.21, N 10.39, S 6.92.

4.4.14. 4.4.14. 1,3-Diethyl-5-((3-(4-nitrophenyl)-1-phenyl-1H-pyrazol-4-yl)methylene)-2-thioxodihydropyrimidine-4,6-(1H,5H)-dione **(6n)**

Yellowish brown solid (88%); m.p.: 228–230 °C; R_f: 0.69 (30% acetone in *n*-hexane); FTIR (ATR, cm^{-1}): 3010 (=C−H), 2939, 2807 (2× C−H), 1710 (C=O), 1619 (C=N), 1561, 1515 (2× C=C); ^{1}H NMR (400 MHz, Chloroform-*d*): δ 9.96 (1H, s, C−$H_{pyrazolyl}$), 8.64 (1H, s, =C−$H_{olefinic}$), 7.98–7.90 (2H, m, Ar-H), 7.71–7.63 (2H, m, Ar-H), 7.58–7.52 (3H, m, Ar-H), 7.51–7.39 (2H, m, Ar-H), 4.64 (2H, q, J = 7.0 Hz, CH_2), 4.59 (2H, q, J = 7.0 Hz, CH_2), 1.38 (3H, t, J = 7.0 Hz, CH_3), 1.32 (3H, t, J = 7.0 Hz, CH_3); ^{13}C NMR (101 MHz, Chloroform-*d*): δ 179.11 (C=S), 161.39 (C=O), 160.12 (C=O), 159.81, 149.45, 139.24, 135.50, 131.06, 129.92, 129.81, 129.25, 128.47, 121.82, 120.42, 116.96, 113.64, 44.32 (CH_2), 43.62 (CH_2), 12.80 (CH_3), 12.65 (CH_3); HRMS (ESI + ve) exact mass calculated for $C_{24}H_{21}N_5O_4S$ $[M+H]^+$: 475.5192, Found: 475.5196; Analysis calculated: C 60.62, H 4.45, N 14.73, S 6.74; Found: C 60.67, H 4.41, N 14.77, S 6.78.

4.5. Enzyme inhibition studies

4.5.1. Cell transfection with lhuman APs and NPPs

The plasmids expressing human APs (TNAP and IAP) [33] or NPPs (NPP1 and NPP3) [34,35] were transfected with COS-7 in 10 cm plates using lipofectamine, as previously reported [33]. The confluent cells (80–90%) were incubated at 37 °C for 5 h in Dulbecco's modified Eagle's medium (DMEM) (without fetal bovine serum (FBS)) with 6 μg of plasmid DNA and 24 μL of lipofectamine reagent. Transfection was stopped by adding DMEM/F-12 containing 20% FBS and cells were harvested after 40–72 h.

4.5.2. Preparation of membrane fractions

The transfected cells (obtained in the previous step) were washed three times with tris-saline buffer at 4 °C. The cells were subsequently collected by scraping in the harvesting buffer (95 mM NaCl, 0.1 mM phenylmethylsulfonyl fluoride (PMSF) and 45 mM tris-buffer) at pH 7.5. The cells were washed twice by centrifugation at 300*g* for 5 min at 4 °C [36]. The obtained cells were resuspended in the harvesting buffer containing 10 μg/mL aprotinin and sonicated. Cellular and nuclear debris were discarded after 10 min centrifugation (300*g* at 4 °C). Glycerol (final concentration of 7.5%) was added to the resulting supernatant and the samples were stored at −80 °C until used. Bradford microplate assay was used for the estimation of protein concentration using bovine serum albumin as a reference standard [37].

4.5.3. Alkaline phosphatase inhibition assay

The alkaline phosphatase (*h*-TNAP and *h*-IAP) inhibition potential of the synthesized compounds was determined using a previously reported method [38]. The compounds were tested at the final concentration of 100 μM, prepared in 10% DMSO. Total volume of 50 μL contained 10 μL of test compound and *h*-TNAP (46 ng/well) or of *h*-IAP (57 ng/well). The reaction mixture was incubated for 5 min at 37 °C and the luminescence signals were measured using microplate reader (BioTek FLx800, USA). After that, 20 μL of CDP-star® substrate was added and reaction was allowed to incubate again for 15 min at the same temperature. The change in luminescence signals was measured and the activity of each compound was compared with total activity control (without any inhibitor). The compounds exhibiting 50% inhibition of either *h*-TNAP or *h*-IAP isozymes were further evaluated for their IC_{50} values. Each experiment was carried out in triplicate. The inhibitory values (IC_{50} values) were calculated using the non-linear regression analysis of program PRISM 5.0 (GraphPad, San Diego, California, USA).

4.5.4. Nucleotide pyrophosphatase inhibition assay

The inhibitory effect of all the derivatives on nucleotide pyrophosphatase (*h*-NPP1 & *h*-NPP3) was determined according to a previously reported method [30]. The total assay volume of 100 μL contained 70 μL of 50 mM tris-HCl (pH 9.5) buffer, 10 μL of the test compound solution (at 0.1 mM final concentration), 10 μL of *h*-NPP1 (final conc. of 27 ng) or *h*-NPP3 (final conc. of 25 ng). The reaction mixture was incubated for 10 min at 37 °C and absorbance was measured at 405 nm using microplate reader (BioTek ELx800, Instruments, Inc. USA). Then, 10 μL of substrate and *p*-nitrophenyl-5′-thymidine monophosphate (*p*-Nph-5-TMP, 0.5 mM), was added to initiate the reaction and the mixture was allowed to incubate at 37 °C for 30 min. The change in absorbance was measured. The compounds that exhibited over 50% inhibition of enzyme activity were further selected for evaluation of their IC_{50} values. All the experiments were carried out in triplicate. The IC_{50} values were calculated using non-linear regression analysis of program PRISM 5.0 (GraphPad, San Diego, California, USA).

4.6. Molecular docking methodology

4.6.1. Selection of protein structure

Due to the unavailability of crystal structures of the targeted enzymes (human alkaline phosphatases and nucleotide pyrophosphatases), the docking studies were carried out in the homology models generated by our group [30–32]. MOE site finder parameter was applied to find out the binding pocket inside respective enzyme, keeping in mind the importance of catalytic zinc ions and magnesium ions inside the active site pocket of enzyme [39]. The structures of these proteins were protonated by AMBER99 force field and minimization was done at root mean square deviation gradient of 0.05 kcal/mol [40].

4.6.2. Preparation of the ligands

The MOE builder tool was used to generate the 3D structures of the compounds [39]. After addition of hydrogen atoms to the compounds, the energy minimization of generated 3D molecules was carried out using MMFF94x force field at the root mean square deviation of 0.01 kcal/mol Å [40].

4.6.3. Docking experiment

The docking analysis was carried out using LeadIT (BioSolveIT GmbH, Germany) [41], after the compound and proteins preparation. The docking analysis and studies were carried out for the selected inhibitors and reference standards without modifying the default parameters. Top 50 ranking poses were visualized and selected for each ligand and further analysis was done using HYDE assessment to investigate the favorable and unfavorable interactions [42]. Poses with lowest binding energy and favorable affinity were chosen and further analyzed by Discovery Studio Visualizer [43].

4.7. Anticancer activity

4.7.1. Cytotoxicity assay (MTT assay)

In vitro cytotoxic activity of the synthetic compounds was evaluated against the breast cancer cells, *i.e.,* MCF-7, and lymphoblast cells from bone-marrow, *i.e.,* K-562 cells, using MTT (dimethyl-2-thiazolyl-2,5-diphenyl-2*H*-tetrazolium bromide)-based cell viability assay, originally described by Mosmann [44] and later modified by Niks and Otto [45]. For the cytotoxicity assay, 90 µL of the culture containing 2.5×10^4 cells/mL was seeded/well in 96-well flat-bottom plates. Then, 10 µL of test compound solution (at final concentration of 100 µM) was added to the respective wells and plates were allowed to incubate for 24 h at 25 ± 1 °C. The well containing only 100 µL culture medium without any compound, drug or cells, was taken as blank. Carboplatin was used as a standard drug. After incubation, 10 µL of MTT was added to each well and plates were again incubated for 4 h at 25 ± 1 °C. Afterwards, 100 µL of quenching reagent (50% isopropanol and 50 mL of 10% sodium dodecylsulfate) was added to stop the enzyme reaction. The plates were incubated for additional 30 min under agitation at room temperature. Absorbance was measured at 570 nm subtracting the background measurement at 690 nm, using 96-well microplate reader. The absorbance of the formazan produced by the action of mitochondrial dehydrogenases of metabolically active cells was correlated with the number of viable cells. The results reported were mean of three independent experiments (± SEM) and expressed as percent inhibitions calculated by the formula:

$$\text{Inhibition}\,(\%) = 100 - \left[\frac{\text{absorbance of the test compounds}}{\text{absorbance of the control}}\right] \times 100$$

IC_{50} values of potential inhibitors were determined with the help of non-linear regression analysis program of GraphPad prism 5.0 (Software Inc., San Diego, California, USA).

4.8. Mechanism of inhibition

In order to characterize the interaction of most potent inhibitors of human TNAP, IAP, NPP1 and NNP3, the type of inhibition was determined using Michaelis–Menten kinetics. For this purpose, the initial rates of the enzyme inhibition were measured at different substrate concentrations in the absence and presence of different concentrations of selected representative inhibitors against respective enzymes. The results were depicted as double reciprocal Lineweaver-Burk plots using PRISM 5.0 (GraphPad, San Diego, California, USA).

Acknowledgements

H.A. is grateful to the Higher Education Commission of Pakistan for financial support under Indigenous 5000 Ph.D Fellowship program. We are also grateful to the DAAD (Programm Deutsch-Pakistanische Hochschulzusammenarbeit) for financial support. J.I. is thankful to the Organization for the Prohibition of Chemical Weapons (OPCW), The Hague, The Netherlands and Higher Education Commission of Pakistan for the financial support through Project No. 20-3733/NRPU/R&D/14/520. A.E is thankful to Sidra Hassan for her help in cell-based assays. J.S. was supported by grants from the Canadian Institutes of Health Research. J. S. is also a recipient of a “Chercheur National” Scholarship award from the “Fonds de recherche du Québec-Santé” (FRQS).

Appendix A. Supplementary material

Supplementary data to this article can be found online at https://doi.org/10.1016/j.bioorg.2019.03.067.

References

[1] a) M. Al-Rashida, J. Iqbal, Therapeutic potentials of ecto-nucleoside triphosphate diphosphohydrolase, ecto-nucleotide pyrophosphatase/phosphodiesterase, ecto-5'-nucleotidase, and alkaline phosphatase inhibitors, Med. Res. Rev. 703–43 (2014); b) C. Stefan, S. Jansen, M. Bollen, Modulation of purinergic signaling by NPP-type ectophosphodiesterases, Purinergic Signal 2 (2006) 361–370.
[2] M. Bollen, R. Gijsbers, H. Ceulemans, W. Stalmans, C. Stefan, Nucleotide pyrophosphatases/phosphodiesterases on the move, Crit. Rev. Biochem. Mol. Biol. 35 (2000) 393–432.
[3] S.-Y. Lee, A. Perotti, S. De Jonghe, P. Herdewijn, T. Hanck, C.E. Müller, Thiazolo[3,2-a]benzimidazol-3(2*H*)-one derivatives: structure-activity relationships of selective nucleotide pyrophosphatase/phosphodiesterase1 (NPP1) inhibitors, Bioorg. Med. Chem. 24 (2016) 3157–3165.
[4] H. Zimmermann, M. Zebisch, N. Sträter, Cellular function and molecular structure of ecto-nucleotidases, Purinergic Signal 8 (2012) 437–502.
[5] L. Chang, S.-Y. Lee, P. Leonczak, J. Rozenski, S. De Jonghe, T. Hanck, C.E. Müller, P. Herdewijn, Imidazopyridine-and purine-thioacetamide derivatives: potent inhibitors of nucleotide pyrophosphatase/phosphodiesterase 1 (NPP1), J. Med. Chem. 57 (2014) 10080–10100.
[6] M.I. Choudhary, N. Fatima, K.M. Khan, S. Jalil, New biscoumarin derivatives-cytotoxicity and enzyme inhibitory activities, Bioorg. Med. Chem. 14 (2006) 8066–8072.
[7] S.-Y. Lee, C.E. Müller, Nucleotide pyrophosphatase/phosphodiesterase 1 (NPP1) and its inhibitors, Med. Chem. Commun. 8 (2017) 823–840.
[8] G. Le Goff, M.T. Martin, C. Servy, S. Cortial, P. Lopes, A. Bialecki, J. Smadja, J. Ouazzani, Isolation and characterization of α, β-unsaturated γ-lactono-hydrazides from Streptomyces sp, J. Nat. Prod. 75 (2012) 915–919.
[9] (a) J.L. Millan, T. Manes, Seminoma-derived Nagao isozyme is encoded by a germ-cell alkaline phosphatase gene, Proc. Natl. Acad. Sci. USA 85 (1988) 3024–3028; (b) J.L. Millán, Alkaline phosphatases: Structure, substrate specificity and functional relatedness to other members of a large superfamily of enzymes, Purinergic Signal 2 (2006) 335–1334; (c) C.R. Greenberg, J.A. Evans, S. McKendry-Smith, S. Redekopp, J.C. Haworth, R. Mulivor, B.N. Chodirker, Infantile hypophosphatasia: localization within chromosome region 1p36.1-34 and prenatal diagnosis using linked DNA markers, Am. J. Hum. Genet. 46 (1990) 286–292.
[10] (a) P. De Prada, J. Loveland-Curtze, J.E. Brenchley, Production of two extracellular alkaline phosphatases by a psychrophilic arthrobacter strain, Appl. Environ. Microbiol. 62 (1996) 3732–3738; (b) A. Ghosh, P.C. Sil, Anti-oxidative effect of a protein from Cajanus indicus L against acetaminophen-induced hepato-nephro toxicity, J. Biochem. Mol. Biol. 40 (2007) 1039–1049; (c) E.E. Kim, H.W. Wyckoff, Reaction mechanism of alkaline phosphatase based on crystal structures. Two-metal ion catalysis, J. Mol. Biol. 218 (1991) 449–464.
[11] M. Al-Rashida, J. Iqbal, Inhibition of alkaline phosphatase: an emerging new drug target, Mini Rev. Med. Chem. 15 (2015) 41–51.
[12] M.C. Yadav, A.M.S. Simao, S. Narisawa, C. Huesa, M.D. McKee, C. Farquharson, J.L. Millán, Loss of skeletal mineralization by the simultaneous ablation of PHOSPHO1 and alkaline phosphatase function: a unified model of the mechanisms of initiation of skeletal calcification, J. Bone Min. Res. 26 (2011) 286–297.
[13] J.S. Whitehouse, K.M. Riggle, D.P. Purpi, A.N. Mayer, K.A. Pritchard, K.T.D. Oldham, M. Gourlay, The protective role of intestinal alkaline phosphatase in necrotizing enterocolitis, J. Surg. Res. 163 (2010) 79–85.
[14] J.P. Lallès, Intestinal alkaline phosphatase: multiple biological roles in maintenance of intestinal homeostasis and modulation by diet, Nutr. Rev. 68 (2010) 323–332.
[15] K. Johnson, J. Goding, D. Van Etten, A. Sali, S.I. Hu, D. Farley, H. Krug, L. Hessle, J.L. Millán, R. Terkeltaub, Linked deficiencies in extracellular PP(i) and osteopontin mediate pathologic calcification associated with defective PC-1 and ANK expression, J. Bone. Miner. Res. 18 (2003) 994–1004.
[16] J.B. Vincent, M.W. Crowder, B. Averill, Hydrolysis of phosphate monoesters: a biological problem with multiple chemical solutions, Trends Biochem. Sci. 17 (1992) 105–110.
[17] D.A. Towler, Inorganic pyrophosphate: a paracrine regulator of vascular calcification and smooth muscle phenotype, Arterioscler. Thromb. Vasc. Biol. 25 (2005) 651–654.
[18] M. Haarhaus, V. Brandenburg, K. Kalantar-Zadeh, P. Stenvinkel, P. Magnusson, Alkaline phosphatase: a novel treatment target for cardiovascular disease in CKD, Nat. Rev. Nephrol. 429–442 (2017).
[19] J.B. Welsh, L.M. Sapinoso, S.G. Kern, D.A. Brown, T. Liu, A.R. Bauskin, R.L. Ward, N.J. Hawkins, D.I. Quinn, P.J. Russell, R.L. Sutherland, Large-scale delineation of secreted protein biomarkers overexpressed in cancer tissue and serum, Proc. Nat. Acad. Sci. 100 (2003) 3410–3415.
[20] R. Dahl, E.A. Sergienko, Y. Su, Y.S. Mostofi, L. Yang, A.M. Simao, S. Narisawa, B. Brown, A. Mangravita-Novo, M. Vicchiarelli, L.H. Smith, Discovery and validation of a series of aryl sulfonamides as selective inhibitors of tissue-nonspecific alkaline phosphatase (TNAP), J. Med. Chem. 52 (2009) 6919–6925.
[21] Comprehensive Heterocyclic Chemistry II vol. 3, (1996) 1.
[22] V. Kumar, K. Kaur, G.K. Gupta, A.K. Sharma, Pyrazole containing natural products: synthetic preview and biological significance, Eur. J. Med. Chem. 69 (2013) 735–753.
[23] K.L. Kees, J.J. Fitzgerald, K.E. Steiner, J.F. Mattes, B. Mihan, T. Tosi, D. Mondoro, M.L. McCaleb, New potent antihyperglycemic agents in db/db mice: synthesis and structure-activity relationship studies of (4-substituted benzyl)(trifluoromethyl) pyrazoles and -pyrazolones, J. Med. Chem. 39 (1996) 3920–3928.

[24] E. Badawey, I.M. El-Ashmawey, Nonsteroidal antiinflammatory agents – Part 1: Antiinflammatory, analgesic and antipyretic activity of some new 1-(pyrimidin-2-yl)-3-pyrazolin-5-ones and 2-(pyrimidin-2-yl)-1,2,4,5,6,7-hexahydro-3H-indazol-3-ones, Eur. J. Med. Chem. 33 (1998) 349–361.

[25] a) S.M. Gomha, M.M. Edrees, F.M.A. Altalbawy, Synthesis and characterization of some new bis-pyrazolyl-thiazoles incorporating the thiophene moiety as potent anti-tumor agents, Int. J. Mol. Sci. 17 (2016) 1499;
b) S.M. Gomha, T.A. Salah, A.O. Abdelhamid, Synthesis, characterization, and pharmacological evaluation of some novel thiadiazoles and thiazoles incorporating pyrazole moiety as anticancer agents, Monatsh Chem. 146 (2015) 149–158;
c) E.M.H. Abbas, S.M. Gomha, T.A. Farghaly, M.M. Abdalla, Synthesis of new thiazole derivatives as antitumor agents, Curr. Org. Synth. 13 (2016) 456–465.

[26] a) M.J. Genin, C. Biles, B.J. Keiser, S.M. Poppe, S.M. Swaney, W.G. Tarpley, Y. Yagi, D.L. Romero, Novel 1,5-diphenylpyrazole nonnucleoside HIV-1 reverse transcriptase inhibitors with enhanced activity versus the delavirdine-resistant P236L mutant: lead identification and SAR of 3- and 4-substituted derivatives, J. Med. Chem. 43 (2000) 1034–1040;
b) M. Abdalla, S. Gomha, M. Abd El-Aziz, N. Serag, Synthesis and evaluation of some novel thiazoles and 1,3-thiazines as potent agents against the rabies virus, Turk. J. Chem. 40 (2016) 441–453.

[27] S.M. Gomha, K.M. Dawood, Synthetic utility of pyridinium bromide: synthesis and antimicrobial activity of novel 2,4,6-trisubstituted pyridines having pyrazole moiety, J. Heterocycl. Chem. 54 (2017) 1943–1948.

[28] A. Saeed, S.A. Ejaz, A. Khurshid, S. Hassan, M. al-Rashida, M. Latif, J. Lecka, J. Sévigny, J. Iqbal, Synthesis, characterization and biological evaluation of N-(2,3-dimethyl-5-oxo-1-phenyl-2,5-dihydro-1*H*-pyrazol-4-yl)benzamides, RSC Adv. 5 (2015) 86428–86439.

[29] H. Andleeb, T. Tehseen, S.J.A. Shah, I. Khan, J. Iqbal, S. Hameed, Identification of novel pyrazole–rhodanine hybrid scaffolds as potent inhibitors of aldose reductase: design, synthesis, biological evaluation and molecular docking analysis, RSC Adv. 6 (2016) 77688–77700.

[30] E. Ausekle, S.A. Ejaz, S.U. Khan, P. Ehlers, A. Villinger, J. Lecka, J. Sévigny, J. Iqbal, P. Langer, New one-pot synthesis of N-fused isoquinoline derivatives by palladium-catalyzed C-H arylation: potent inhibitors of nucleotide pyrophosphatase-1 and -3, Org. Biomol. Chem. 14 (2016) 11402–11414.

[31] I. Khan, A. Ibrar, S.A. Ejaz, S.U. Khan, S.J.A. Shah, S. Hameed, J. Simpson, J. Lecka, J. Sévigny, J. Iqbal, Influence of the diversified structural variations at the imine functionality of 4-bromophenylacetic acid derived hydrazones on alkaline phosphatase inhibition: synthesis and molecular modelling studies, RSC Adv. 5 (2015) 90806–90811.

[32] B. Jafari, N. Yelibayeva, M. Ospanov, S.A. Ejaz, S. Afzal, S.U. Khan, Z.A. Abilov, M.Z. Turmukhanova, S.N. Kalugin, S. Safarov, J. Lecka, J. Sévigny, J.Q. Rahman, P. Ehlers, J. Iqbal, P. Langer, Synthesis of 2-arylated thiadiazolopyrimidones by Suzuki-Miyaura cross-coupling: a new class of nucleotide pyrophosphatase (NPPs) inhibitors, RSC Adv. 6 (2016) 107556–107571.

[33] Y. Bravo, P. Teriete, R.-P. Dhanya, R. Dahl, P.S. Lee, T. Kiffer-Moreira, S.R. Ganji, E. Sergienko, L.H. Smith, C. Farquharson, Design, synthesis and evaluation of benzoisothiazolones as selective inhibitors of PHOSPHO1, Bioorg. Med. Chem. Lett. 24 (2014) 4308–4311.

[34] S.I. Belli, J.W. Goding, Biochemical characterization of human PC-1, an enzyme possessing alkaline phosphodiesterase I and nucleotide pyrophosphatase activities, Eur. J. Biochem. 226 (1994) 433–443.

[35] P. Jinhua, J.W. Goding, H. Nakamura, K. Sano, Molecular cloning and chromosomal localization of PD-Ibeta (PDNP3), a new member of the human phosphodiesterase I genes, Genomics 45 (1997) 412–415.

[36] F. Kukulski, S.A. Lévesque, E.G. Lavoie, J. Lecka, F. Bigonnesse, A.F. Knowles, S.C. Robson, T.L. Kirley, J. Sévigny, Comparative hydrolysis of P2 receptor agonists by NTPDases 1, 2, 3 and 8, Purinergic Signal 1 (2005) 193–204.

[37] M.M. Bradford, A rapid and sensitive method for the quantitation of microgram quantities of protein utilizing the principle of protein-dye binding, Anal. Biochem. 72 (1976) 248–254.

[38] E.A. Sergienko, J.L. Millán, High-throughput screening of tissue-nonspecific alkaline phosphatase for identification of effectors with diverse modes of action, Nat. Prot. 5 (2010) 1431–1439.

[39] MOE (Molecular Operating Environment) Version 2014.0901. Chemical Computing Group, (CCG). http://www.chemcomp.com/MOEMolecular_Operating_Environment.htm.

[40] Labute, P. Protonate 3D: Assignment of Macromolecular Protonation State and Geometry, Chemical Computing Group, 2007. http://www.chemcomp.com/journal/proton.htm.

[41] LeadIT, 2014, at http://www.biosolveit.de/LeadIT.

[42] N. Schneider, G. Lange, S. Hindle, R. Klein, M. Rarey, A consistent description of HYdrogen bond and DEhydration energies in protein-ligand complexes: methods behind the HYDE scoring function, J. Comput. Aided Mol. Des. 27 (2013) 15–29.

[43] Accelrys Software Inc., Discovery Studio Modeling Environment, Release 4.0, Accelrys Software, San Diego, CA, 2013.

[44] T. Mosmann, Rapid colorimetric assay for cellular growth and survival: application to proliferation and cytotoxicity assays, J. Immunol. Meth. 65 (1983) 55–63.

[45] M. Niks, M. Otto, Towards an optimized MTT assay, J. Immunol. Meth. 130 (1990) 149–151.